A Kernel-Free Boundary Integral Method for 2-D Magnetostatics Analysis

Zichao Jin[1], Yue Cao[2], Shuwang Li[2], Wenjun Ying[3], and Mahesh Krishnamurthy[1]

[1]Department of Electrical and Computer Engineering, Illinois Institute of Technology, Chicago, IL 60616 USA
[2]Department of Applied Mathematics, Illinois Institute of Technology, Chicago, IL 60616 USA
[3]Institute of Natural Sciences and School of Mathematical Sciences, Shanghai Jiao Tong University, Shanghai 200240, China

Performing magnetostatic analysis accurately and efficiently is very important for multi-objective optimization of electromagnetic device designs. In this research, a kernel-free boundary integral method (KFBIM) has been introduced for solving magnetic computations in a toroidal core geometry in 2-D. This study is very relevant in the design and optimization of toroidal inductors or transformers used in electrical systems, where lighter weight, higher inductance, higher efficiency, and lower leakage flux are required. The governing partial differential equations (PDEs) have been formulated as a system of the Fredholm integral equations of the second kind. Unlike traditional boundary integral methods or boundary element methods, KFBIM does not require an analytical form of Green's function for evaluating integrals via numerical quadrature. Instead, KFBIM computes integrals by solving an equivalent interface problem on a Cartesian mesh. Compared with traditional finite difference methods for solving the governing PDEs directly, KFBIM produces a well-conditioned linear system. Therefore, the KFBIM requires only a fixed number of iterations when an iterative method [e.g., generalized minimal residual method (GMRES)] is applied for solving the linear system, and the numerical solution is not sensitive to computer round-off errors. The obtained results are then compared with a commercial finite element solver (ANSYS), which shows excellent agreement. It should be noted that, compared with FEM, the KFBIM does not require a body-fit mesh and can achieve high accuracy with a coarse mesh. In particular, the calculations of the magnetic potential and the tangential field intensity on the boundaries are more stable and exhibit almost no oscillations.

Index Terms— **Boundary element method (BEM), boundary integral method, finite element method (FEM), magnetostatics analysis, toroidal core.**

I. INTRODUCTION

MULTI-OBJECTIVE optimization of electromagnetic designs has gained considerable attention over the last few decades, and one of the most important parts is to solve magnetostatics problems accurately and as rapidly as possible. Numerical methods have been utilized for solving magnetostatics problems over the past few decades, and several significant advancements have been made. These approaches can carry out magnetic analysis for almost all device geometries with the desired accuracy. Of the various commercial tools available, finite element methods (FEMs) have led numerical analysis tools for electric machines, such as ANSYS Maxwell [1] and COMSOL ac/dc module [2]. Although FEM is a very powerful tool, the computational cost tends to be high, making it difficult to meet the efficiency goal when solving machine design problems. The main challenge in using FEM in optimization applications is the requirement of volumetric mesh on the entire domain. This meshing stage requires significant computational resources even for simple topologies, especially when: 1) small geometries require high mesh resolution irrespective of whether these geometries are important or not and 2) all nodes must be shared among elements. In other words, nodes are usually not allowed to be placed along an element edge, so large amount of data is required as input for the mesh used in terms of nodal connectivity. In addition, the body fit mesh is adopted, which means that the mesh depends on the shape of the domains, as shown in Fig. 1 (left). As a result, the domain needs to be re-meshed for every design.

To overcome several of these drawbacks, integral methods have been introduced to mitigate the meshing challenges of FEM, such as the boundary element method (BEM) and method of moments (MOM) [12], [13], [14], [15], [16], [17], [18], [19], [20]. The boundary integral method can treat the boundary or interface conditions exactly and is usually considered to be the most accurate method, provided that well-developed accurate and stable quadrature of boundary integrals are available [21], [22], [23]. Moreover, after integral formulations, the dimensionality of the homogeneous partial differential equation (PDE) problem is reduced by one. Namely, a 2-D domain problem can be solved via the integration on a 1-D curve; thus, the computational cost is reduced dramatically.

For solving electromagnetics problems, unlike the FEM that solves differential equations, the BEM and MOM solve integral formations of PDEs using magnetic potentials. MoM and BEM have several similarities: BEM uses fewer elements in its mesh because it only discretizes the surface or boundary, and therefore, fewer data are required to perform a calculation. However, it has several limitations. First, it is not suitable for nonlinear problems as it is inherently difficult to accommodate inhomogeneities and nonlinearities in the domain interior. Second, it is not straightforward to evaluate a volume integral for a non-homogeneous PDE. Finally, the analytical form of Green's functions for each problem is required to evaluate integrals

Manuscript received 15 November 2022; revised 10 January 2023; accepted 6 February 2023. Date of publication 22 February 2023; date of current version 24 March 2023. Corresponding author: Z. Jin (e-mail: zjin10@hawk.iit.edu).

Color versions of one or more figures in this article are available at https://doi.org/10.1109/TMAG.2023.3247444.

Digital Object Identifier 10.1109/TMAG.2023.3247444

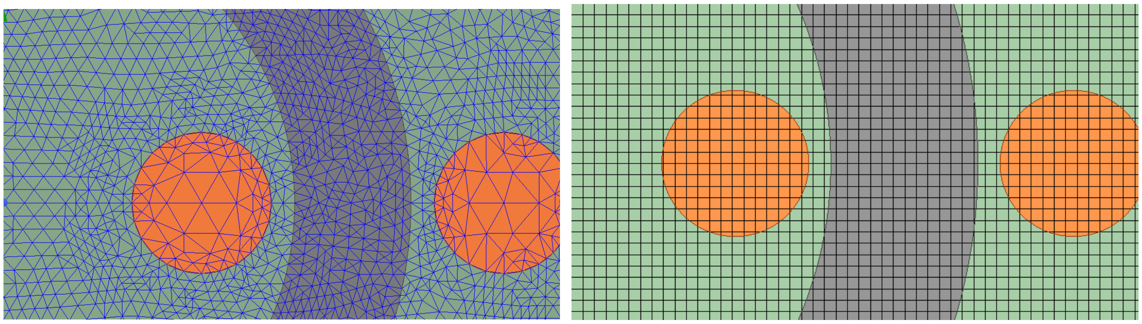

Fig. 1. Body-fit mesh for FEM (left) and mesh for KFBIM (right).

and to solve the problem, which increases the complexity of the problem-solving process for engineers because Green's function is usually not available for complex geometry and PDEs with variable coefficients.

In this article, a kernel-free boundary integral method (KFBIM) has been introduced for electromagnetic analysis, which is a generalization of the traditional boundary integral method and is also a Cartesian grid-based integral method. A unique feature of the KFBIM method is that it does not require the analytic form of Green's function or special quadrature to directly evaluate integrals. Instead, the idea behind KFBIM is to reinterpret boundary integrals as solutions to equivalent simple interface problems posed in a rectangle box, which can be solved efficiently by a finite difference method coupled with numerical corrections (to gain accuracy), FFT-based solution, and interpolations (to gain efficiency). The resulting linear system from the KFBIM approach requires only a fixed number of iterations when an iterative method (e.g., the Krylov subspace-based method) is applied. In addition to the solution of the PDE, the KFBIM also gives a solution for the layer densities on the boundary or interface, which is a useful quantity to consider in practice. Moreover, the KFBIM can solve non-homogeneous elliptic PDEs with variable coefficients. Therefore, KFBIM can be applied in electromagnetics problems with non-homogeneous material properties. It should be noted that, unlike FEM, KFBIM does not require a body-fit mesh when solving integrals, as shown in Fig. 1 (right). Also, unlike the finite difference method for solving a PDE directly, KFBIM is based on the integral formulation (usually the Fredholm integral equations of the second kind), and thus, it always produces a well-conditioned discrete linear system of equations, which is much less sensitive to computer round-off or other errors. In addition, it also gives monopole and dipole densities at the interface, which conventional FEM is unable to provide.

The KFBIM approach has been developed to be a general method for elliptic PDEs in two and three dimensions for single or double boundary [3], [4], [5], [6], [7], [8], [24]. The integrals are solved on a Cartesian grid-based method, e.g., a finite difference scheme, which means that it delivers accurate results using a general grid, and it is not necessary to re-mesh for every design when it is used for optimization. Therefore, it can overcome the major shortcomings of FEM.

In this study, a toroidal core is selected as a candidate for magnetostatic analysis, which is commonly used in a toroidal inductor or transformer design because the magnetic flux is confined in the toroidal core and the inductance is increased [30]. Toroidal inductors and transformers are used in a wide range of circuits: power supplies, inverters, and amplifiers, which are used in lots of electrical systems: TVs, computers, and audio systems because of their lighter weight, higher inductance, higher efficiency, and lower leakage flux. This shape also serves as the foundational structure toward developing a solution for the design and optimization of electric machines. Computation from this approach shows excellent agreement with results from a commercial finite element solver (ANSYS). Compared with FEM, KFBIM can achieve high accuracy with a coarse mesh and produces the results of double- or single-layer densities at the boundary or interface; particularly, the gradient calculation of the tangential field intensity on the inner boundary is more stable and exhibits almost no oscillations.

TABLE I
DIMENSIONS OF TOROIDAL CORE

Region	Dimensions
Air box	20cm × 20cm
Center of Air box	(0,0)
Inner radius of toroidal core	4.5cm
Outer radius of toroidal core	6.5cm
Center of toroidal core	(0,0)
Radius of coil	1.4cm
Centers of 2 coils	(2.7cm, 0) & (8.3cm, 0)
Current	100A

The organization of this article is given as follows. In Section II, linear magnetostatic analysis of the toroidal core is presented. In Section III, the kernel-free boundary integral method for a doubly connected domain has been derived. Section IV presents the methodology to implement the KFBIM for EM design. Section V presents the results from the KFBIM approach and compares the accuracy and efficiency between KFBIM and FEM. In Section VI, this article concludes and discusses potential applications for this new approach.

II. PROBLEM DESCRIPTION OF A TOROIDAL CORE

A. *Geometry of the Toroidal Core*

Fig. 2 shows the toroidal core problem studied in this article. The dimension of the core is summarized in Table I. PDEs

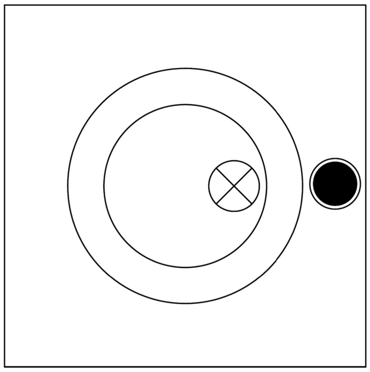

Fig. 2. Toroidal core.

and appropriate boundary conditions governing magnetostatics form the first step in this process.

B. Partial Differential Equations for Magnetostatics and Boundary Conditions

We introduce the magnetic vector potential **A** to solve the magnetic field

$$\mathbf{B} = \mu \mathbf{H} \tag{1}$$

$$\mu \mathbf{H} = \nabla \times \mathbf{A} \tag{2}$$

where **H** is the magnetic field or magnetic field intensity or strength, **B** is the magnetic flux density, and μ is the magnetic permeability.

The PDE for solving **A** is obtained

$$\nabla \times \left(\frac{1}{\mu} \nabla \times \mathbf{A} \right) = \mathbf{J}. \tag{3}$$

In two dimensions, since **A** only has a component on z direction, the equation becomes

$$\nabla \cdot \left(\frac{1}{\mu} \nabla \cdot \mathbf{A}_z \right) = \mathbf{J}_z. \tag{4}$$

It can be written as

$$\nabla \cdot (\nu \nabla \cdot \mathbf{A}_z) = \mathbf{J}_z \tag{5}$$

where ν is the reciprocal of magnetic permeability. The condition on the boundary of the rectangular box is set to be

$$\mathbf{A}_z = 0. \tag{6}$$

In addition, $\mathbf{A}_z$ must satisfy a continuity condition along the normal direction at the air–iron boundaries

$$\nu_0 \left(\frac{\partial \mathbf{A}_z}{\partial n} \right)_{\text{air}} = \nu \left(\frac{\partial \mathbf{A}_z}{\partial n} \right)_{\text{iron}} \tag{7}$$

where ν_0 is the reciprocal of magnetic permeability of air, ν is the reciprocal of magnetic permeability of iron, and n denotes the unit outward normal vector on each interface. Other than the conditions mentioned above, the continuity of the potential **A** across material boundaries is also needed to guarantee that the condition on the normal component of **B** is satisfied.

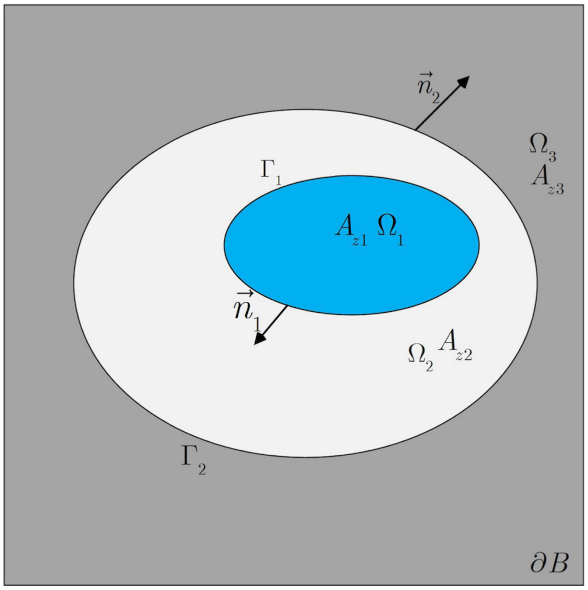

Fig. 3. Schematic diagrams of a doubly connected domain for interface problem.

III. KERNEL-FREE BOUNDARY INTEGRAL METHOD FOR TWO-INTERFACE 2-D MAGNETOSTATICS PROBLEM

In this section, a general KFBIM has been introduced for a two-interface 2-D magnetostatic problem. The toroidal core magnetostatics problem is then reformulated into this KFBIM framework. The formulation and algorithm presented below are extensions of the approach developed recently in [24], and they are reformulated corresponding to the magnetostatics problem in this article. The main steps are outlined here.

Let $\mathcal{B} \subset \mathbb{R}^d (d = 2 \text{ or } 3)$ be a rectangular box. Γ_1 and Γ_2 are smooth interfaces in $\mathcal{B}$ and partition the box into three subdomains, Ω_1, Ω_2, and Ω_3, $\partial\bar{\Omega}_1 \cap \partial\bar{\Omega}_2 = \Gamma_1$, and $\partial\bar{\Omega}_2 \cap \partial\bar{\Omega}_3 = \Gamma_2$, as shown in Fig. 3. Let $\mathbf{p} \in \mathbb{R}^d (d = 2 \text{ or } 3)$ be the space variable. Since the problem is solved in 2-D, all the field variables are independent of z. As shown in Section II, the z components $\mathbf{J}_z$ and $\mathbf{A}_z$ are used to solve the 2-D problem. In this case, $J_{z1}(\mathbf{p})$, $J_{z2}(\mathbf{p})$, and $J_{z3}(\mathbf{p})$ are z components of the current density **J** defined, respectively, in Ω_1, Ω_2, and Ω_3, and they are smooth source functions; A_{z1}, A_{z2}, and A_{z3} are z components of magnetic vector potential **A** defined in Ω_1, Ω_2, and Ω_3, respectively; $\nu(\mathbf{p})$ and $\nu_0(\mathbf{p})$ are the reciprocal of magnetic permeability of iron and air, they can be spatially constant and variable, and the numerical examples are shown in Section V. The 2-D magnetostatics problem can be rewritten as an interface problem

$$\mathcal{A}_1 A_{z1} \equiv \nabla \cdot (\nu_0(\mathbf{p}) \nabla A_{z1}) = -J_{z1}(\mathbf{p}) \quad \text{in } \Omega_1 \tag{8}$$

$$\mathcal{A}_2 A_{z2} \equiv \nabla \cdot (\nu(\mathbf{p}) \nabla A_{z2}) = -J_{z2}(\mathbf{p}) \quad \text{in } \Omega_2 \tag{9}$$

$$\mathcal{A}_3 A_{z3} \equiv \nabla \cdot (\nu_0(\mathbf{p}) \nabla A_{z3}) = -J_{z3}(\mathbf{p}) \quad \text{in } \Omega_3 \tag{10}$$

$$A_{z1} - A_{z2} = 0 \text{ and } \nu_0 \partial_n A_{z1} - \nu \partial_n A_{z2} = 0 \quad \text{on } \Gamma_1 \tag{11}$$

$$A_{z2} - A_{z3} = 0 \text{ and } \nu \partial_n A_{z2} - \nu_0 \partial_n A_{z3} = 0 \quad \text{on } \Gamma_2 \tag{12}$$

$$A_{z3} = 0 \quad \text{on } \partial\mathcal{B} \tag{13}$$

where $\mathcal{A}_i$ is the differential operator (Laplace operator for magnetostatics problem) of PDE in Ω_i $(i = 1, 2, 3)$.

A. Boundary Integrals and Volume Integrals

The boundary integrals and volume integrals are derived from facts of potential theory [6], [25], [26], [27], [28], [29]. Let $G_i(\mathbf{p},\mathbf{q})$ be Green's function associated with the variable coefficients PDE on the rectangle $\mathcal{B}$, at a point $\mathbf{q}$; it satisfies

$$\mathcal{A}_i G_i(\mathbf{p},\mathbf{q}) = \nabla_{\mathbf{p}} \cdot \left(\nu_i(\mathbf{p}) \nabla_{\mathbf{p}} G_i(\mathbf{p},\mathbf{q})\right) = \delta(\mathbf{p}-\mathbf{q}) \quad \text{in } \mathcal{B} \tag{14}$$

$$G_i(\mathbf{p},\mathbf{q}) = 0 \quad \text{on } \partial\mathcal{B} \tag{15}$$

where $\delta(\mathbf{p}-\mathbf{q})$ is the Dirac delta function; $\nabla_{\mathbf{p}}$ stands for the gradient operator with respect to the space variable $\mathbf{p} \in \mathbb{R}^d$.

For interface problem (8)–(13), Green's functions corresponding to the three PDEs are generally different. We consider that $G_1(\mathbf{p},\mathbf{q})$ is Green's function associated with (8) in Ω_1 and satisfies

$$\mathcal{A}_1 G_1(\mathbf{p},\mathbf{q}) = \delta(\mathbf{p}-\mathbf{q}) \quad \text{in } \mathcal{B} \tag{16}$$

$$G_1(\mathbf{p},\mathbf{q}) = 0 \quad \text{on } \partial\mathcal{B}. \tag{17}$$

$G_2(\mathbf{p},\mathbf{q})$ is Green's function associated with (9) in Ω_2 and satisfies

$$\mathcal{A}_2 G_2(\mathbf{p},\mathbf{q}) = \delta(\mathbf{p}-\mathbf{q}) \quad \text{in } \mathcal{B} \tag{18}$$

$$G_2(\mathbf{p},\mathbf{q}) = 0 \quad \text{on } \partial\mathcal{B} \tag{19}$$

and $G_3(\mathbf{p},\mathbf{q})$ is Green's function associated with (10) in Ω_3 and satisfies

$$\mathcal{A}_3 G_3(\mathbf{p},\mathbf{q}) = \delta(\mathbf{p}-\mathbf{q}) \quad \text{in } \mathcal{B} \tag{20}$$

$$G_3(\mathbf{p},\mathbf{q}) = 0 \quad \text{on } \partial\mathcal{B}. \tag{21}$$

Using density functions φ_1 and φ_2, we define double-layer boundary integrals

$$\mathcal{M}_1\varphi_1(\mathbf{p}) = \int_{\Gamma_1} \nu_1(\mathbf{q}) \frac{\partial G_1(\mathbf{p},\mathbf{q})}{\partial \mathbf{n}_{\mathbf{q}}} \varphi_1(\mathbf{q}) ds_{\mathbf{q}} \tag{22}$$

$$\mathcal{M}_2\varphi_1(\mathbf{p}) = \int_{\Gamma_1} \nu_2(\mathbf{q}) \frac{\partial G_2(\mathbf{p},\mathbf{q})}{\partial \mathbf{n}_{\mathbf{q}}} \varphi_1(\mathbf{q}) ds_{\mathbf{q}} \tag{23}$$

$$\mathcal{M}_2\varphi_2(\mathbf{p}) = \int_{\Gamma_2} \nu_2(\mathbf{q}) \frac{\partial G_2(\mathbf{p},\mathbf{q})}{\partial \mathbf{n}_{\mathbf{q}}} \varphi_2(\mathbf{q}) ds_{\mathbf{q}} \tag{24}$$

$$\mathcal{M}_3\varphi_2(\mathbf{p}) = \int_{\Gamma_2} \nu_3(\mathbf{q}) \frac{\partial G_3(\mathbf{p},\mathbf{q})}{\partial \mathbf{n}_{\mathbf{q}}} \varphi_2(\mathbf{q}) ds_{\mathbf{q}}. \tag{25}$$

Using density functions ψ_1 and ψ_2, we define single-layer boundary integrals

$$\mathcal{L}_1\psi_1(\mathbf{p}) = \int_{\Gamma_1} G_1(\mathbf{p},\mathbf{q}) \psi_1(\mathbf{q}) ds_{\mathbf{q}} \tag{26}$$

$$\mathcal{L}_2\psi_1(\mathbf{p}) = \int_{\Gamma_1} G_2(\mathbf{p},\mathbf{q}) \psi_1(\mathbf{q}) ds_{\mathbf{q}} \tag{27}$$

$$\mathcal{L}_2\psi_2(\mathbf{p}) = \int_{\Gamma_2} G_2(\mathbf{p},\mathbf{q}) \psi_2(\mathbf{q}) ds_{\mathbf{q}} \tag{28}$$

$$\mathcal{L}_3\psi_2(\mathbf{p}) = \int_{\Gamma_2} G_3(\mathbf{p},\mathbf{q}) \psi_2(\mathbf{q}) ds_{\mathbf{q}}. \tag{29}$$

The volume integrals are defined as

$$\mathcal{G}_1(-J_{z1}(\mathbf{p})) = \int_{\Omega_1} G_1(\mathbf{p},\mathbf{q})(-J_{z1}(\mathbf{p})) dq \tag{30}$$

$$\mathcal{G}_2(-J_{z2}(\mathbf{p})) = \int_{\Omega_1 \cup \Omega_2} G_2(\mathbf{p},\mathbf{q})(-J_{z2}(\mathbf{p})) dq \tag{31}$$

$$\mathcal{G}_3(-J_{z3}(\mathbf{p})) = \int_{\Omega_3} G_3(\mathbf{p},\mathbf{q})(-J_{z3}(\mathbf{p})) dq. \tag{32}$$

Hypersingular and adjoint double-layer boundary integrals' operators are denoted as $\mathcal{N}_1$, $\mathcal{N}_2$, $\mathcal{N}_3$, $\mathcal{M}_1^*$, $\mathcal{M}_2^*$, and $\mathcal{M}_3^*$

$$\mathcal{N}_1\varphi_1(\mathbf{p}) = \int_{\Gamma_1} \nu_1(\mathbf{p})\nu_1(\mathbf{q}) \frac{\partial^2 G_1(\mathbf{p},\mathbf{q})}{\partial \mathbf{n}_{\mathbf{q}} \partial \mathbf{n}_{\mathbf{p}}} \varphi_1(\mathbf{q}) ds_{\mathbf{q}} \tag{33}$$

$$\mathcal{N}_2\varphi_1(\mathbf{p}) = \int_{\Gamma_1} \nu_2(\mathbf{p})\nu_2(\mathbf{q}) \frac{\partial^2 G_2(\mathbf{p},\mathbf{q})}{\partial \mathbf{n}_{\mathbf{q}} \partial \mathbf{n}_{\mathbf{p}}} \varphi_1(\mathbf{q}) ds_{\mathbf{q}} \tag{34}$$

$$\mathcal{N}_2\varphi_2(\mathbf{p}) = \int_{\Gamma_1} \nu_2(\mathbf{p})\nu_2(\mathbf{q}) \frac{\partial^2 G_2(\mathbf{p},\mathbf{q})}{\partial \mathbf{n}_{\mathbf{q}} \partial \mathbf{n}_{\mathbf{p}}} \varphi_2(\mathbf{q}) ds_{\mathbf{q}} \tag{35}$$

$$\mathcal{N}_3\varphi_2(\mathbf{p}) = \int_{\Gamma_1} \nu_2(\mathbf{p})\nu_2(\mathbf{q}) \frac{\partial^2 G_3(\mathbf{p},\mathbf{q})}{\partial \mathbf{n}_{\mathbf{q}} \partial \mathbf{n}_{\mathbf{p}}} \varphi_2(\mathbf{q}) ds_{\mathbf{q}} \tag{36}$$

$$\mathcal{M}_1^*\psi_1(\mathbf{p}) = \int_{\Gamma_1} \nu_1(\mathbf{p}) \frac{\partial G_1(\mathbf{p},\mathbf{q})}{\partial \mathbf{n}_{\mathbf{q}}} \psi_1(\mathbf{q}) ds_{\mathbf{q}} \tag{37}$$

$$\mathcal{M}_2^*\psi_1(\mathbf{p}) = \int_{\Gamma_1} \nu_2(\mathbf{p}) \frac{\partial G_2(\mathbf{p},\mathbf{q})}{\partial \mathbf{n}_{\mathbf{q}}} \psi_1(\mathbf{q}) ds_{\mathbf{q}} \tag{38}$$

$$\mathcal{M}_2^*\psi_2(\mathbf{p}) = \int_{\Gamma_2} \nu_2(\mathbf{p}) \frac{\partial G_2(\mathbf{p},\mathbf{q})}{\partial \mathbf{n}_{\mathbf{q}}} \psi_2(\mathbf{q}) ds_{\mathbf{q}} \tag{39}$$

$$\mathcal{M}_3^*\psi_2(\mathbf{p}) = \int_{\Gamma_2} \nu_3(\mathbf{p}) \frac{\partial G_3(\mathbf{p},\mathbf{q})}{\partial \mathbf{n}_{\mathbf{q}}} \psi_2(\mathbf{q}) ds_{\mathbf{q}}. \tag{40}$$

B. Formulation of Boundary Integral Equations

Let $\mathcal{B} \subset \mathbb{R}^2$ be a rectangular box. $\Omega_1 \subset R^2$ is a bounded domain with smooth boundary Γ_1 [see Fig. 4(a)]. The domain outside Γ_1 is denoted as $\overline{\Omega}_1^c$. $A_{z1}(x,y)$ and $A_{z2}(x,y)$ are unknown functions, as the solutions to an interface problem

$$\mathcal{A}_1 A_{z1} \equiv \nabla \cdot (\nu_1(\mathbf{p}) \nabla A_{z1}) = -J_{z1}(\mathbf{p}) \quad \text{in } \Omega_1 \tag{41}$$

$$\mathcal{A}_2 A_{z2} \equiv \nabla \cdot (\nu_2(\mathbf{p}) \nabla A_{z2}) = 0 \quad \text{in } \overline{\Omega}_1^c \tag{42}$$

$$A_{z1} - A_{z2} = g_1' \text{ and } \nu_1 \partial_n A_{z1} - \nu_2 \partial_n A_{z2} = j_1' \quad \text{on } \Gamma_1 \tag{43}$$

$$A_{z2} = 0 \quad \text{on } \partial\mathcal{B} \tag{44}$$

where $\Omega_2' \subset R^2$ is a bounded domain with a smooth boundary Γ_2 [see Fig. 4(b)]. The domain outside Γ_2 is denoted as Ω_3. $A_{z2}'(x,y)$ and $A_{z3}(x,y)$ are unknown functions, as the solutions to another interface problem

$$\mathcal{A}_2 A_{z2}' \equiv \nabla \cdot \left(\nu_2(\mathbf{p}) \nabla A_{z2}'\right) = -J_{z2}(\mathbf{p}) \quad \text{in } \Omega_2' \tag{45}$$

$$\mathcal{A}_3 A_{z3} \equiv \nabla \cdot (\nu_3(\mathbf{p}) \nabla A_{z3}) = -J_{z3}(\mathbf{p}) \quad \text{in } \Omega_3 \tag{46}$$

$$A_{z2}' - A_{z3} = g_2' \text{ and } \nu_1 \partial_n A_{z2}' - \nu_2 \partial_n A_{z3} = j_2' \quad \text{on } \Gamma_2 \tag{47}$$

$$A_{z3} = 0 \quad \text{on } \partial\mathcal{B}. \tag{48}$$

Here, both interfaces Γ_1 and Γ_2, PDE operators $\mathcal{A}_1$, $\mathcal{A}_2$, and $\mathcal{A}_3$, and source terms J_{z1}, J_{z2}, and J_{z3} are the same as interface problems (8)–(13). $\overline{\Omega}_1^c = \Omega_2 \cup \Omega_3 \cup \Gamma_2$. $\Omega_2' = \Omega_1 \cup \Omega_2 \cup \Gamma_1$. However, interface conditions g_1', j_1', g_2', and j_2' are different from the interface conditions in (11) and (12), and they are not necessarily required for the KFBIM. The solution to the first interface problem is

$$A_{z1}(\mathbf{p}) = \mathcal{M}_1\varphi_1(\mathbf{p}) - \mathcal{L}_1\psi_1(\mathbf{p}) + \mathcal{G}_1(-J_{z1}) \quad \text{in } \Omega_1 \tag{49}$$

$$A_{z2}(\mathbf{p}) = \mathcal{M}_2\varphi_1(\mathbf{p}) - \mathcal{L}_2\psi_1(\mathbf{p}) \quad \text{in } \overline{\Omega}_1^c \tag{50}$$

and the solution to the second interface problem is

$$A_{z2}'(\mathbf{p}) = \mathcal{M}_2\varphi_2(\mathbf{p}) - \mathcal{L}_2\psi_2(\mathbf{p}) + \mathcal{G}_1(-J_{z2}) \quad \text{in } \Omega_2' \tag{51}$$

$$A_{z3}(\mathbf{p}) = \mathcal{M}_3\varphi_3(\mathbf{p}) - \mathcal{L}_3\psi_3(\mathbf{p}) + \mathcal{G}_1(-J_{z3}) \quad \text{in } \Omega_3. \tag{52}$$

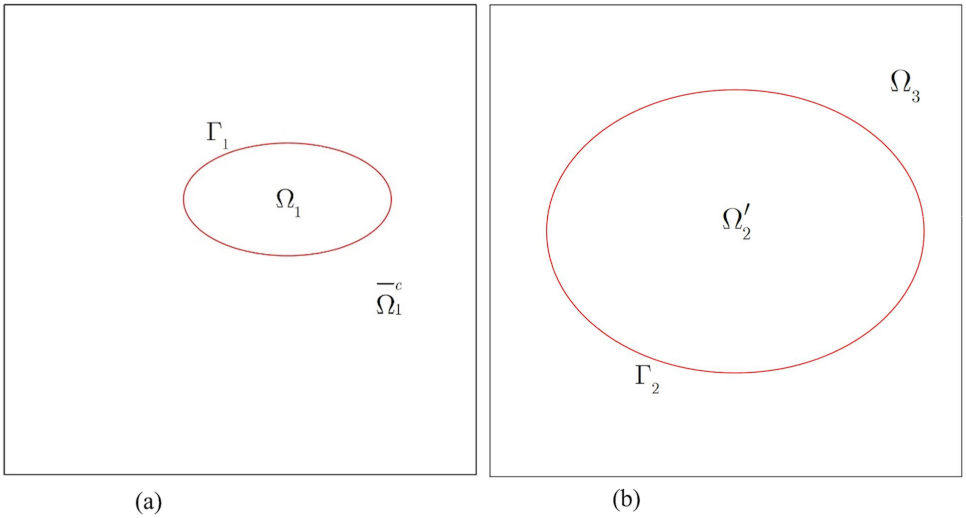

Fig. 4. Illustration of the two interface problems. (a) Exterior problem. (b) Interior problem.

We have four boundary integral equations on Γ_1 and Γ_2 by interface conditions (11) and (12)

$$(\mathcal{M}_1-\mathcal{M}_2+\mathcal{I})\varphi_1+(\mathcal{L}_2-\mathcal{L}_1)\psi_1-\mathcal{M}_2\varphi_2+\mathcal{L}_2\psi_2 = g_1-\mathcal{G}_1(-J_{z1})+\mathcal{G}_2(-J_{z2}) \quad \text{on } \Gamma_1 \tag{53}$$

$$(\mathcal{N}_1-\mathcal{N}_2)\varphi_1+\left(\mathcal{M}_2^*-\mathcal{M}_1^*+\mathcal{I}\right)\psi_1-\mathcal{N}_2\varphi_2+\mathcal{M}_2^*\psi_2 = j_1-\mathbf{n_p}\cdot\sigma_1\nabla_{\mathbf{p}}\mathcal{G}_1(-J_{z1})+\mathbf{n_p}\cdot\sigma_2\nabla_{\mathbf{p}}\mathcal{G}_2(-J_{z2}) \quad \text{on } \Gamma_1 \tag{54}$$

$$\mathcal{M}_2\varphi_1-\mathcal{L}_2\psi_1+(\mathcal{M}_2-\mathcal{M}_3+\mathcal{I})\varphi_2+(\mathcal{L}_3-\mathcal{L}_2)\psi_2 = g_2-\mathcal{G}_2(-J_{z2})+\mathcal{G}_3(-J_{z3}) \quad \text{on } \Gamma_2 \tag{55}$$

$$\mathcal{N}_2\varphi_1-\mathcal{M}_2^*\psi_1+(\mathcal{N}_2-\mathcal{N}_3)\varphi_2+\left(\mathcal{M}_3^*-\mathcal{M}_2^*+\mathcal{I}\right)\psi_2 = j_2-\mathbf{n_p}\cdot\sigma_2\nabla_{\mathbf{p}}\mathcal{G}_2(-J_{z2})+\mathbf{n_p}\cdot\sigma_3\nabla_{\mathbf{p}}\mathcal{G}_3(-J_{z3}) \quad \text{on } \Gamma_2. \tag{56}$$

In the matrix form, the above integral equations can be written as in (57), shown at the bottom of the page, where

$$\begin{pmatrix} r_1 \\ r_2 \\ r_3 \\ r_4 \end{pmatrix} = \begin{pmatrix} g_1-\mathcal{G}_1(-J_{z1})+\mathcal{G}_2(-J_{z2}) \\ j_1-\mathbf{n_p}\cdot\sigma_1\nabla_{\mathbf{p}}\mathcal{G}_1(-J_{z1})+\mathbf{n_p}\cdot\sigma_2\nabla_{\mathbf{p}}\mathcal{G}_2(-J_{z2}) \\ g_2-\mathcal{G}_2(-J_{z2})+\mathcal{G}_3(-J_{z3}) \\ j_2-\mathbf{n_p}\cdot\sigma_2\nabla_{\mathbf{p}}\mathcal{G}_2(-J_{z2})+\mathbf{n_p}\cdot\sigma_3\nabla_{\mathbf{p}}\mathcal{G}_3(-J_{z3}) \end{pmatrix}. \tag{58}$$

Here, the notation is $\partial_{\mathbf{p}} = \mathbf{n_p}\cdot\nabla_{\mathbf{p}}$. After solving the above linear system by generalized minimal residual method (GMRES) [21], [22], the final solution A_z to the interface problem is given by

$$A_z(\mathbf{p}) = A_{z1}(\mathbf{p}) \quad \text{in } \Omega_1 \tag{59}$$

$$A_z(\mathbf{p}) = A_{z2}(\mathbf{p})+A_{z2}'(\mathbf{p}) \quad \text{in } \Omega_2 \tag{60}$$

$$A_z(\mathbf{p}) = A_{z3}(\mathbf{p}) \quad \text{in } \Omega_3. \tag{61}$$

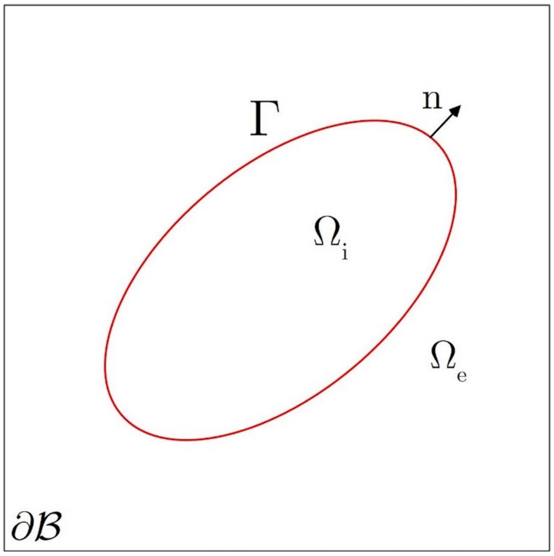

Fig. 5. Irregular domain with the exterior domain Ω_e and the interior domain Ω_i.

Then, the flux density can be calculated by $B(\mathbf{p}) = \text{curl}A_z(\mathbf{p})$ or

$$B_x(\mathbf{p}) = \frac{\partial A_z(\mathbf{p})}{\partial y} \tag{62}$$

$$B_y(\mathbf{p}) = -\frac{\partial A_z(\mathbf{p})}{\partial x}. \tag{63}$$

C. Evaluation of Boundary or Volume Integral

In general, Green's function used in boundary integrals is not available for elliptic PDEs with variable coefficients.

$$\begin{pmatrix} \mathcal{M}_1-\mathcal{M}_2+\mathcal{I} & \mathcal{L}_2-\mathcal{L}_1 & -\mathcal{M}_2 & \mathcal{L}_2 \\ \mathcal{N}_1-\mathcal{N}_2 & \mathcal{M}_2^*-\mathcal{M}_1^*+\mathcal{I} & -\mathcal{N}_2 & \mathcal{M}_2^* \\ \mathcal{M}_2 & -\mathcal{L}_2 & \mathcal{M}_2-\mathcal{M}_3+\mathcal{I} & \mathcal{L}_3-\mathcal{L}_2 \\ \mathcal{N}_2 & -\mathcal{M}_2^* & \mathcal{N}_2-\mathcal{N}_3 & \mathcal{M}_3^*-\mathcal{M}_2^*+\mathcal{I} \end{pmatrix} \begin{pmatrix} \varphi_1 \\ \psi_1 \\ \varphi_2 \\ \psi_2 \end{pmatrix} = \begin{pmatrix} r_1 \\ r_2 \\ r_3 \\ r_4 \end{pmatrix} \tag{57}$$

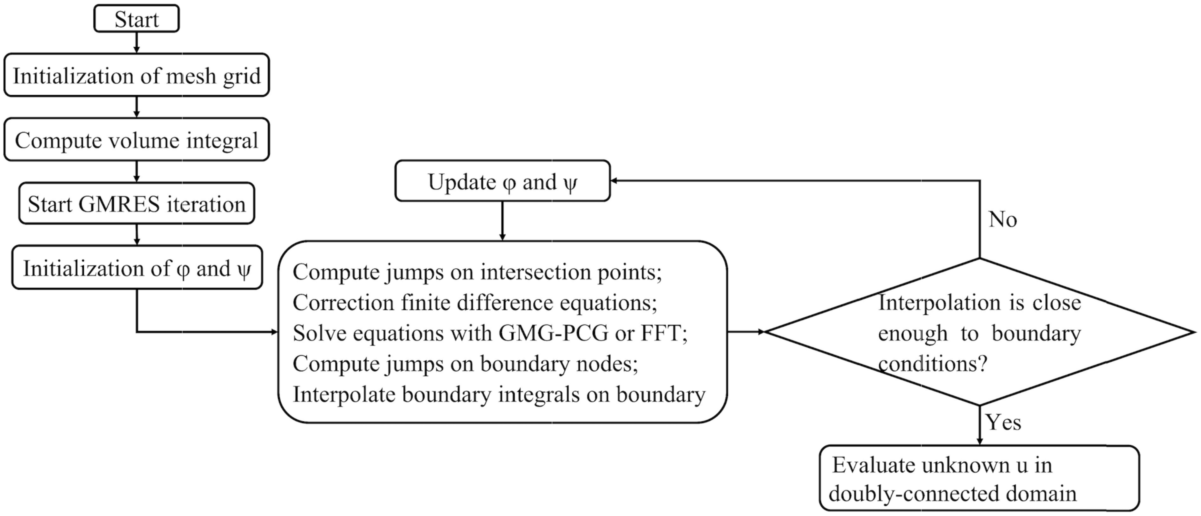

Fig. 6. Flowchart of the overall algorithm.

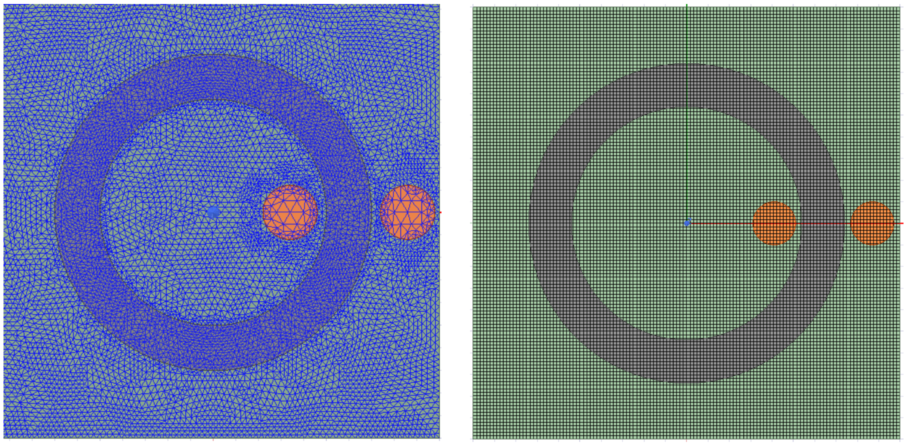

Fig. 7. FEM mesh (left) and KFBIM (right) mesh for the toroidal core.

The KFBIM circumvents the direct evaluation of boundary integrals and computes the value of boundary or volume integrals as an interpolation of Cartesian grid value from a discretized equivalent interface problem.

1) Reinterpretation of Integrals: By the continuity properties of the boundary and volume integrals, we may reinterpret each of them as a solution to an equivalent interface problem.

In a rectangular box $\mathcal{B}$, an irregular interface Γ separates it into two domains Ω_i and Ω_e (see Fig. 5 for an illustration). A piecewise smooth function $w(\mathbf{p})$ is defined in $\mathcal{B}$, which has possible discontinuity only on the interface Γ. We denote $w^+(\mathbf{p})$ and $w^-(\mathbf{p})$ as the restriction of $w(\mathbf{p})$ in Ω_i and Ω_e, respectively. When $\mathbf{p} \in \Gamma$, $w^+(\mathbf{p})$ and $w^-(\mathbf{p})$ mean the limit values of $w(\mathbf{p})$ from the interior domain Ω_i and the exterior domain Ω_e, respectively. It is assumed the interior domain Ω_i is on the positive side of the interface Γ, while the exterior domain Ω_e is on the negative side. The possible discontinuity is described as jumps in the function $w(\mathbf{p})$ across the domain boundary from the negative side to the positive side, which is denoted by

$$\big[w(\mathbf{p})\big] = w^+(\mathbf{p}) - w^-(\mathbf{p}) \quad \text{on } \Gamma. \tag{64}$$

Using the jumps defined above, the double-layer boundary $v(\mathbf{p}) = \mathcal{M}_{i,e}\varphi(\mathbf{p})$ satisfies an interface problem

$$\mathcal{A}_{i,e}v \equiv \nabla \cdot \big(\nu_{i,e}(\mathbf{p})\nabla v\big) = 0 \quad \text{in } \mathcal{B}\backslash\Gamma \tag{65}$$

$$[v] = \varphi \quad \text{on } \Gamma \tag{66}$$

$$\big[\nu_{i,e}\partial_{\mathbf{n}}v\big] = 0 \quad \text{on } \Gamma \tag{67}$$

$$v = 0 \quad \text{on } \partial\mathcal{B} \tag{68}$$

and the single-layer boundary integral $v(\mathbf{p}) = -\mathcal{L}_{i,e}\psi(\mathbf{p})$ satisfies an interface problem

$$\mathcal{A}_{i,e}v \equiv \nabla \cdot \big(\nu_{i,e}(\mathbf{p})\nabla v\big) = 0 \quad \text{in } \mathcal{B}\backslash\Gamma \tag{69}$$

$$[v] = 0 \quad \text{on } \Gamma \tag{70}$$

$$\big[\nu_{i,e}\partial_{\mathbf{n}}v\big] = \psi \quad \text{on } \Gamma \tag{71}$$

$$v = 0 \quad \text{on } \partial\mathcal{B}. \tag{72}$$

Finally, the volume integral $v(\mathbf{p}) = \mathcal{G}_i(-J_{zi}(\mathbf{p}))$ satisfies the following interface problem:

$$\mathcal{A}_i v \equiv \nabla \cdot (\nu_i(\mathbf{p})\nabla v) = -J_{zi} \quad \text{in } \Omega_i \tag{73}$$

$$\mathcal{A}_e v = 0 \quad \text{in } \Omega_e \tag{74}$$

$$[v] = 0 \quad \text{on } \Gamma \tag{75}$$

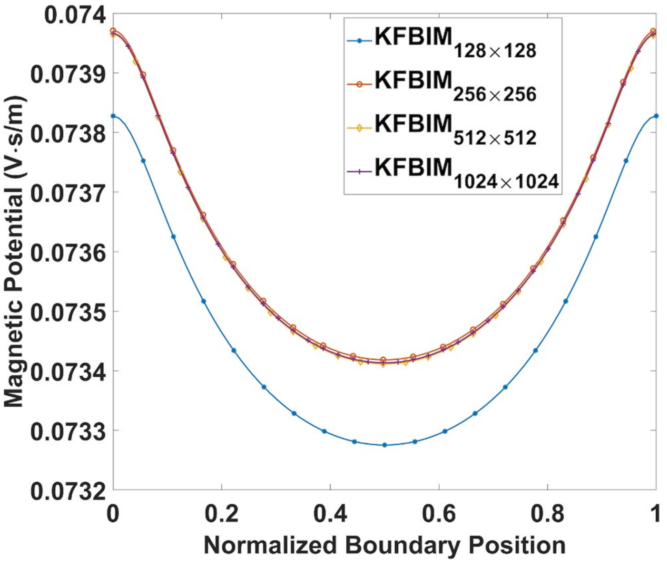

Fig. 8. Comparison of the magnetic potential on the inner boundary between KFBIM on different grids for Example 1.

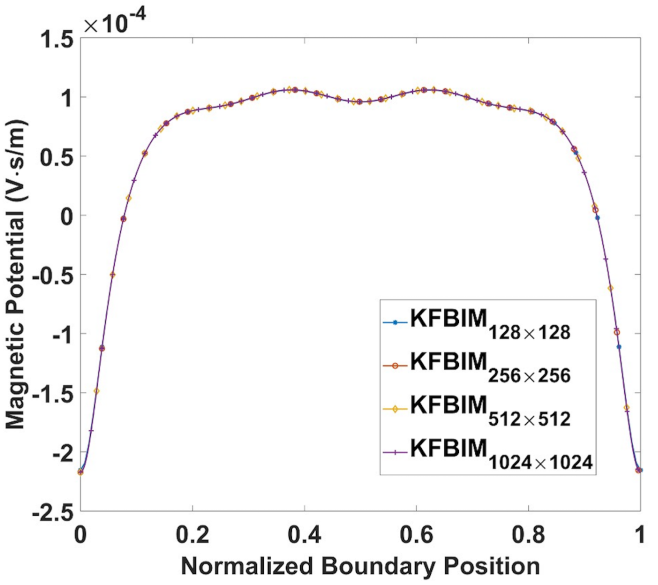

Fig. 9. Comparison of the magnetic potential on the outer boundary between KFBIM on different grids for Example 1.

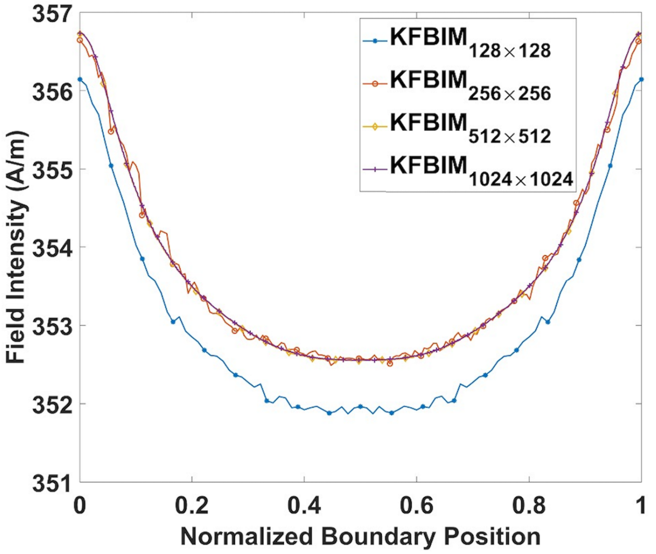

Fig. 10. Comparison of the tangential field intensity on the inner boundary between KFBIM on different grids for Example 1.

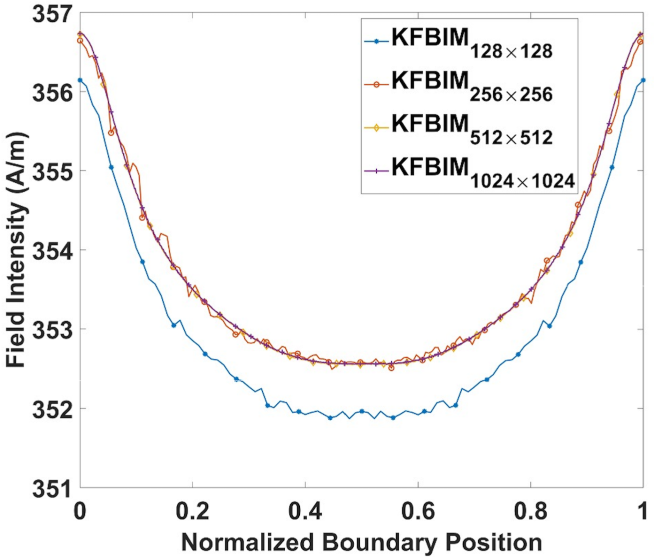

Fig. 11. Comparison of the tangential field intensity on the outer boundary between KFBIM on different grids for Example 1.

$$[\nu_i \partial_{\mathbf{n}} v] = 0 \quad \text{on } \Gamma \tag{76}$$

$$v = 0 \quad \text{on } \partial\mathcal{B}. \tag{77}$$

The volume integral $v(\mathbf{p}) = \mathcal{G}_e(-J_{ze}(\mathbf{p}))$ satisfies the following interface problem:

$$\mathcal{A}_i v = 0 \quad \text{in } \Omega_i \tag{78}$$

$$\mathcal{A}_e v \equiv \nabla \cdot (\nu_e(\mathbf{p})\nabla v) = -J_{ze} \quad \text{in } \Omega_e \tag{79}$$

$$[v] = 0 \quad \text{on } \Gamma \tag{80}$$

$$[\nu_e \partial_{\mathbf{n}} v] = 0 \quad \text{on } \Gamma \tag{81}$$

$$v = 0 \quad \text{on } \partial\mathcal{B} \tag{82}$$

where Ω_i and Ω_e are the interior domain and the exterior domain of certain boundaries, and boundary or volume integrals are defined the same as those used in Sections III-A and III-B; J_{zi} and J_{ze} are current densities on the interior domain and the exterior domain. The equivalence between the interface problem and boundary or volume integrals can be found in [7] and [24]. Technical details for solving the integrals have been included in the Appendix, including PDE discretization, correction in the discrete system, solution of the discrete finite difference equations, interpolation of integrals on the interface, and computation of jumps of partial derivatives [6], [7], [8].

In summary, the given PDE problem is first decomposed problems into two interface problems and then rewritten into a linear system [see (53)–(56)] using well-defined single- or double-layer integrals. These integrals are then solved on a Cartesian grid-based method, e.g., a finite difference approach. To improve the accuracy of the integral evaluation, corrections are only made for points near the interface. The

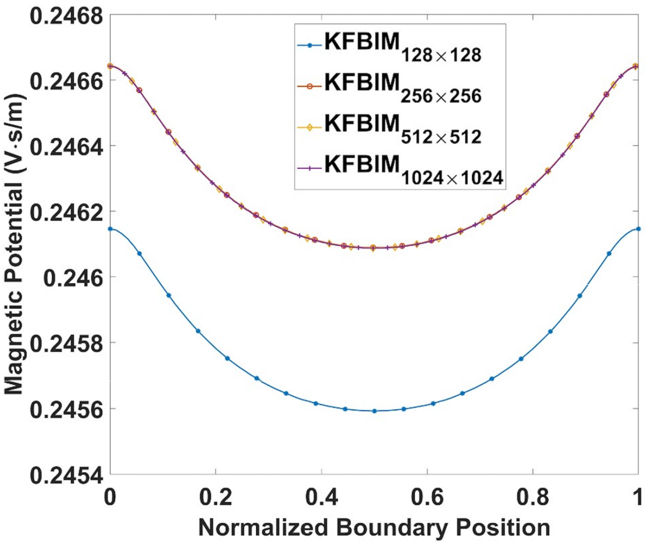

Fig. 12. Comparison of the magnetic potential on the inner boundary between KFBIM on different grids for Example 2.

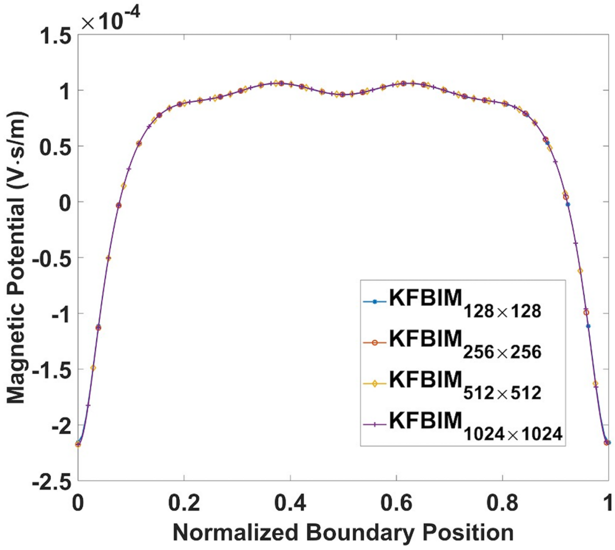

Fig. 13. Comparison of the magnetic potential on the outer boundary between KFBIM on different grids for Example 2.

resulting linear system is solved iteratively using a Krylov subspace method (GMRES) [10], [11]. During each iteration, a geometric multigrid preconditioned conjugate gradient method (GMG-PCG) is used to solve the equivalent interface problem [see (65)–(82)]. These simple equivalent interface problems (65)–(82) are solved using Appendices A–C. The correction in Appendix B for the discrete interface equations needs the jumps of partial derivatives, which are computed by the method presented in Appendix E. After the discrete equations are solved, the grid-based solution is interpolated to the interface using Appendix D, which also needs the jumps of partial derivatives calculated by the method in Appendix E. The following algorithm is used for solving the interface problem [see (8)–(13)]. As mentioned previously, the jumps of partial derivatives are the possible discontinuities of partial derivatives on the boundary in a function. The flowchart of the overall algorithm is shown in Fig. 6.

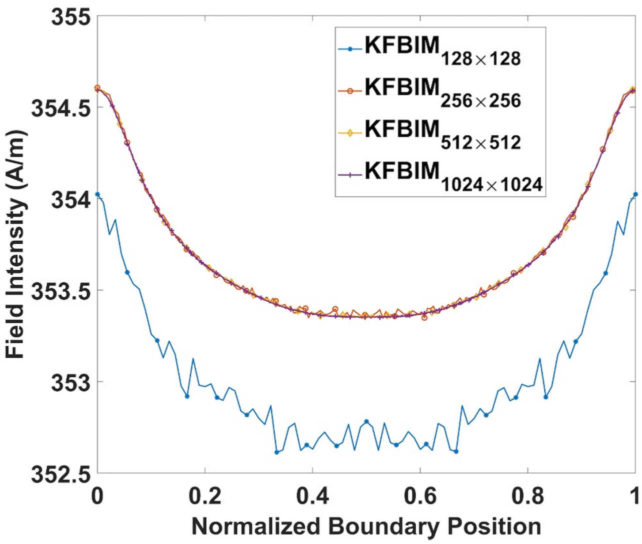

Fig. 14. Comparison of the tangential field intensity on the inner boundary between KFBIM on different grids for Example 2.

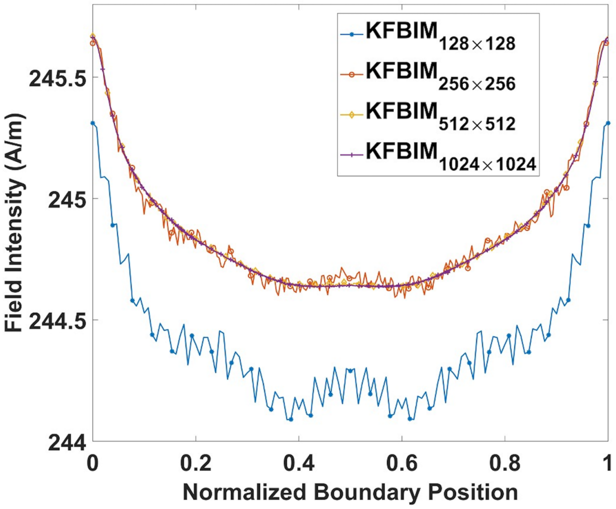

Fig. 15. Comparison of the tangential field intensity on the outer boundary between KFBIM on different grids for Example 2.

IV. IMPLEMENTING THE KFBIM

KFBIM is a non-dimensional approach. Therefore, to solve the toroidal core problem, the first step is to de-unitize the problem. The characteristic length is selected to be 10 cm. Thus, the nondimensional rectangular box is 2×2, the inner radius is 0.45, and the outer radius is 0.65. The radius of current sources is 0.14, and centers are located at (0.27, 0) and (0.83, 0). The material in Ω_1 and Ω_3 is air, and the material in Ω_2 is the iron. For the permeability of air, it is set to be constant permeability of free space, which is $4\pi \times 10^{-7}$. For the permeability of iron, there are two setting in our study: for the first case, the relative permeability of iron is 1000; for the other case, the iron is treated as an inhomogeneous permeable material, and the relative permeability is $(5000/1 + 2(x^2 + y^2)) + 200$ to test the ability of KFBIM to solve nonhomogeneous electromagnetic problem. Following

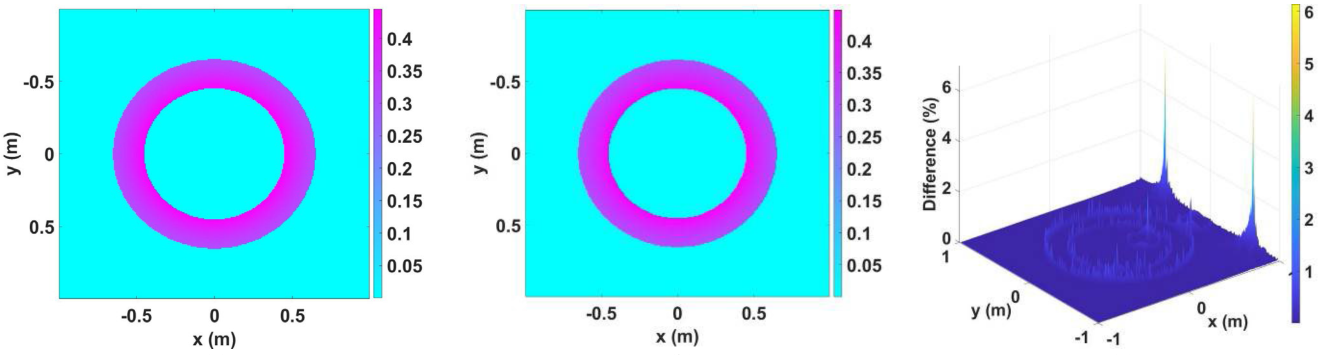

(a) (b) (c)

Fig. 16. Comparison of flux density results for coarsest mesh. (a) Flux density results from KFBIM (256 × 256). (b) Flux density results from FEM on the coarsest mesh (16 129 elements). (c) Difference of the flux density between FEM on coarsest mesh (16 129 elements) and KFBIM for Example 1.

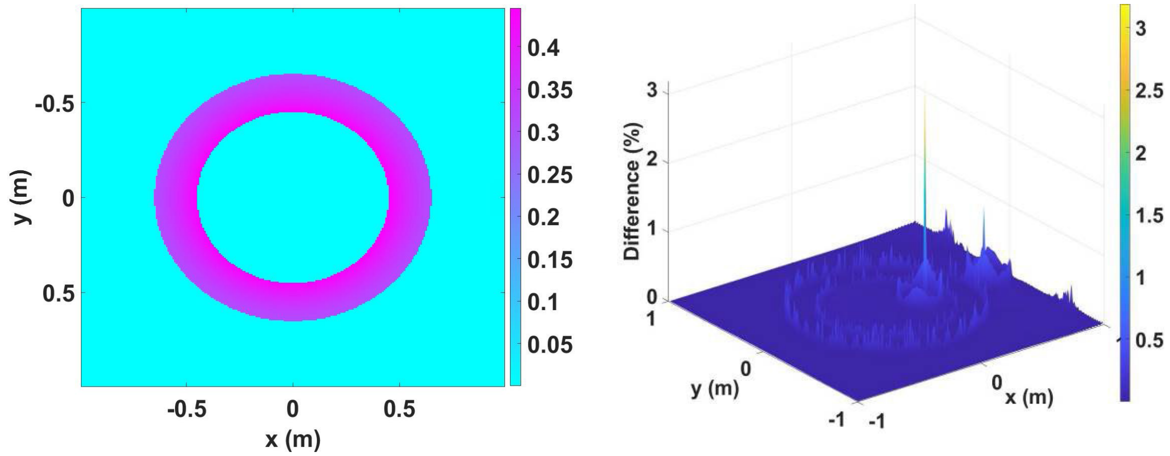

(a) (b)

Fig. 17. Comparison of flux density results for coarser mesh. (a) Flux density results from FEM on coarser mesh (65 025 elements). (b) Difference of the flux density between FEM on coarser mesh (65 025 elements) and KFBIM for Example 1.

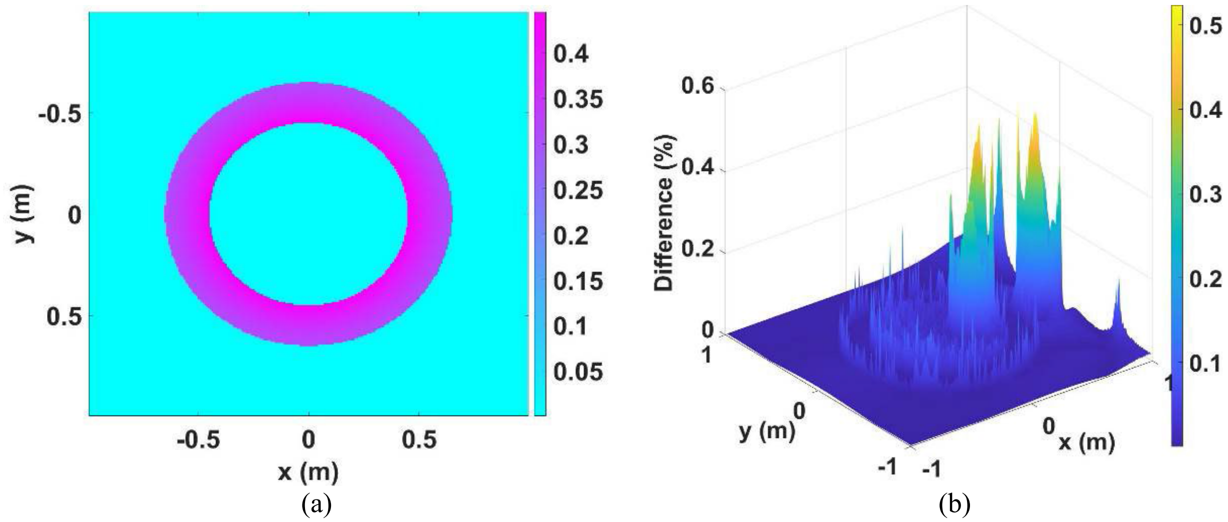

(a) (b)

Fig. 18. Comparison of flux density results for dense mesh. (a) Flux density results from FEM on dense mesh (261 121 elements). (b) Difference of the flux density between FEM on dense mesh (261 121 elements) and KFBIM for Example 1.

the general framework of KFBIM discussed in Section III, the source function J_z is defined as followings.

In the EM package of commercially available FE software, the current value or current density is assigned to the coil, which is 100 A and 162 403 A/m^2 (1000 and 16 240.3 after nondimensionalization), and the zero current is applied to iron for this case. In the KFBIM approach, $J_{z2}(x, y)$ is 0 on Ω_2, and smooth Sigmoid functions are used to evenly model distributed

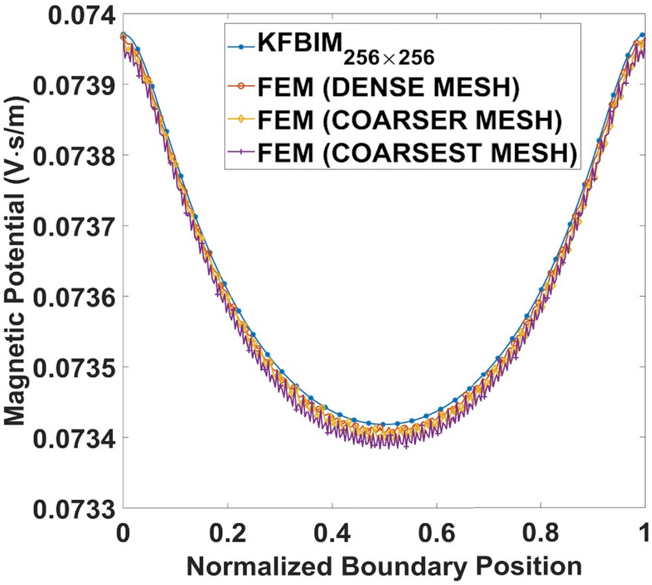

Fig. 19. Comparison of the magnetic potential on the inner boundary between KFBIM (256 × 256) (almost no oscillations) and FEM (more oscillations) for Example 1.

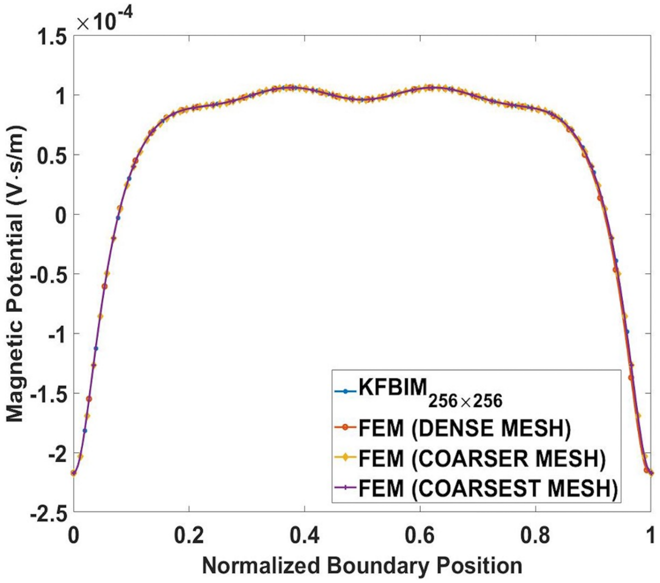

Fig. 20. Comparison of the magnetic potential on the outer boundary between KFBIM (256 × 256) and FEM for Example 1.

current source flow through the coil. Mathematically, we take

$$J_{z1}(x,y)=\frac{16241.0}{1+\exp\left\{35.0\left(\frac{(x-0.27)^2}{0.14^2}+\frac{y^2}{0.14^2}\right)-1\right\}} \tag{83}$$

and

$$J_{z3}(x,y)=-\frac{16241.0}{1+\exp\left\{35.0\left(\frac{(x-0.83)^2}{0.14^2}+\frac{y^2}{0.14^2}\right)-1\right\}}. \tag{84}$$

Note that the integration of the above Sigmoid functions in the domain is 1000, which is exactly the value after the de-unitization of 100 A. The shape of these two functions is very close to cylinders located at the coils of the original problem.

V. KFBIM RESULTS AND COMPARISON WITH FEM

A. *FEM Mesh Configuration*

In this study, FEM forms the baseline of numerical electromagnetic problems in terms of accuracy and computational efficiency, which is carried out using a commercial package, ANSYS Electronics. In the software, the 2-D electromagnetics problems are solved using the Maxwell 2-D package.

In the Maxwell 2-D software, a 2-D triangular adaptive uniform (TAU) mesher is used, which generates a fully automated initial mesh. TAU creates a uniform, high-quality, solver-driven mesh and can be instructed to refine the mesh by reducing the length of elements. Three conditions are considered—a dense mesh with 268 535 elements; a coarser mesh with 68 439 elements; and the coarsest mesh with 16 027 elements. The reason for choosing these three meshes is that they have similar resolutions for KFBIM, which corresponds to 261 121, 65 025, and 16 129 elements on 512 × 512, 256 × 256, and 128 × 128 grids, respectively, to have a fair comparison. The meshed geometry is shown in Fig. 7.

B. *KFBIM Results*

This section starts with a comparison of KFBIM results solved on 1024 × 1024, 512 × 512, 256 × 256, and 128 × 128 grids. It is understood that, if the values on the boundary converge, the values on the whole domain converge. Therefore, the values solved on the boundary, vector potential, and tangential field intensity are compared.

Example 1 (Spatially Constant Permeability): For the first example, the relative permeability on the toroidal core is spatially constant 1000, as mentioned in Section IV. The vector potential comparisons on inner and outer boundaries are shown in Figs. 8 and 9. The tangential field intensity comparisons on inner and outer boundaries are shown in Figs. 10 and 11.

Example 2 (Nonhomogeneous Permeable Material): For this example, the relative permeability on the toroidal core is spatially variable $(5000/1+2(x^2+y^2))+200$, as mentioned in Section IV. The vector potential comparisons for inner and outer boundaries are shown in Figs. 12 and 13. The tangential field intensity comparisons for inner and outer boundaries are shown in Figs. 14 and 15.

Based on the comparisons of boundary values of the two examples, it is clear that the problems start to converge when it is solved on the 256 × 256 grid. The values solved on the 256 × 256 grid are very close to the 512 × 512 grid and the 1024 × 1024 grid. Since the 256 × 256 case is the most computationally efficient between these three cases without losing accuracy, it is taken as an example to be compared with FEM in terms of accuracy of flux density on the whole domain and boundary values.

C. *Accuracy Comparison*

Example 1 (Spatially Constant Permeability): For the first example, the relative permeability on the toroidal core is spatially constant 1000, as mentioned in Section IV. The

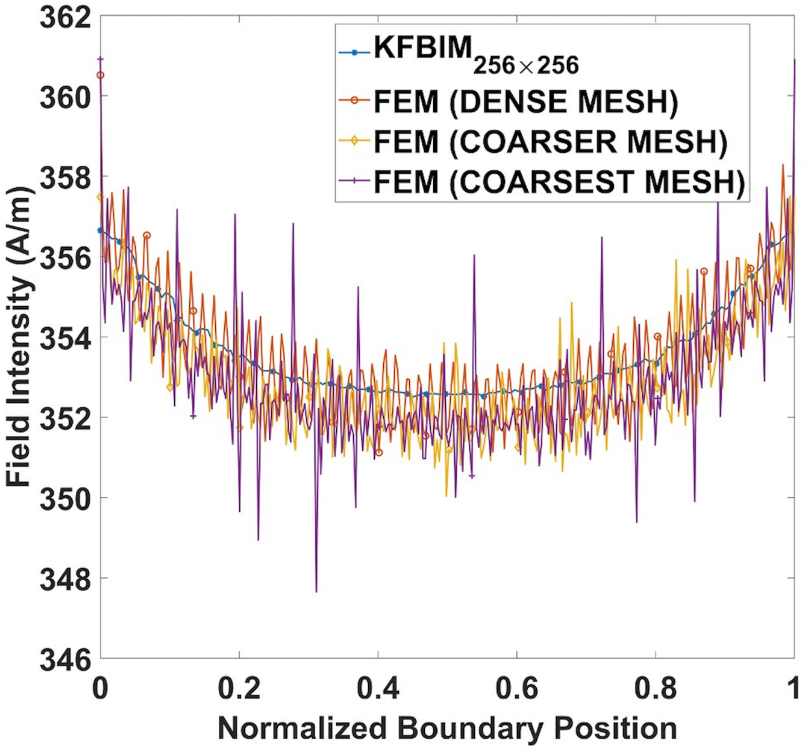

Fig. 21. Comparison of the tangential field intensity on the inner boundary between KFBIM (256 × 256) (almost no oscillations) and FEM (more oscillations) for Example 1.

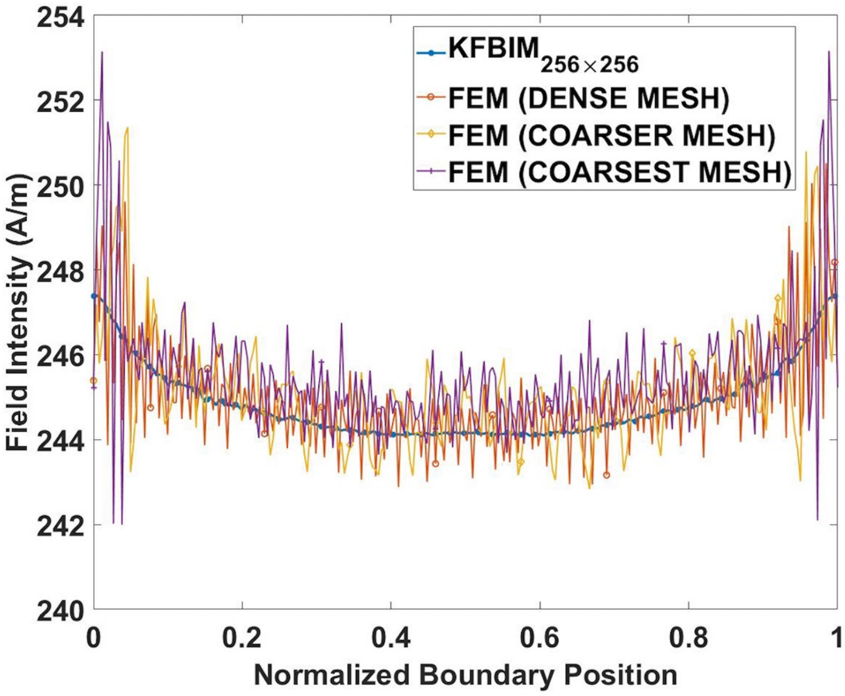

Fig. 22. Comparison of the tangential field intensity on the outer boundary between KFBIM (256 × 256) (almost no oscillations) and FEM (more oscillations) for Example 1.

magnitude of flux density is compared for each point first. The magnetostatics problem is solved using KFBIM on a 256 × 256 grid. For FEM, the problem is solved for each condition, i.e., from the coarsest mesh to the densest mesh. Figs. 16–18 compare the accuracy of the calculations for each point on the 256 × 256 grid. The comparison is done between KFBIM and FEM using three different meshes, and the maximum differences are 6.14%, 3.18%, and 0.52%, respectively. The difference is calculated by

$$\text{Difference}_k = \frac{|B_{k,\text{FEM}} - B_{k,\text{KFBIM}}|}{B_{k,\text{FEM}}}. \tag{85}$$

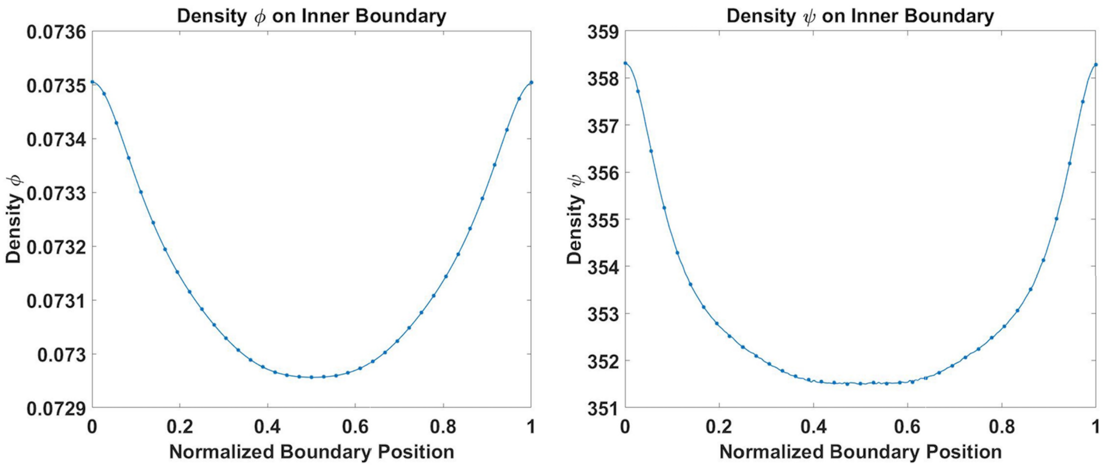

Fig. 23. Densities on the inner and outer boundaries computed by KFBIM for Example 1.

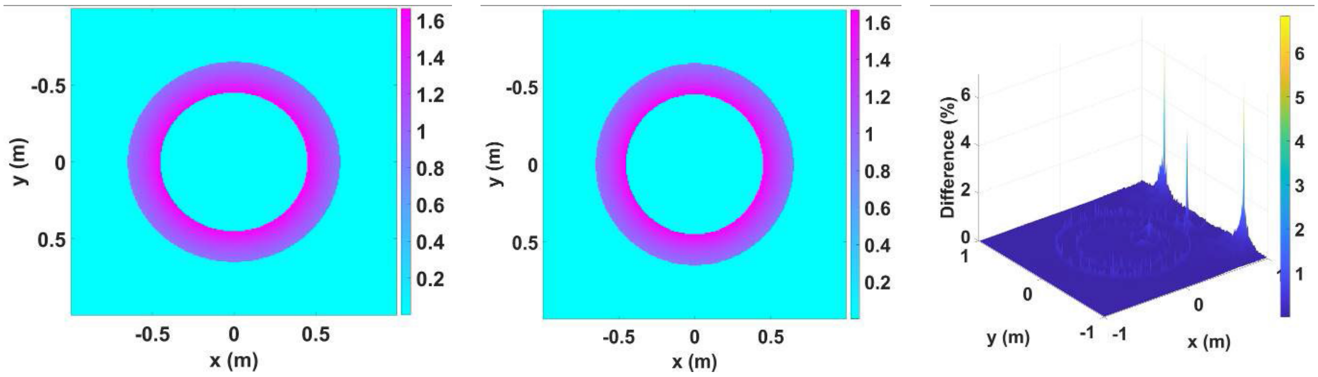

(a) (b) (c)

Fig. 24. Comparison of flux density results for coarsest mesh. (a) Flux density results from KFBIM (256 × 256). (b) Flux density results from FEM on the coarsest mesh (16 129 elements). (c) Difference of the flux density between FEM on coarsest mesh (16 129 elements) and KFBIM for Example 2.

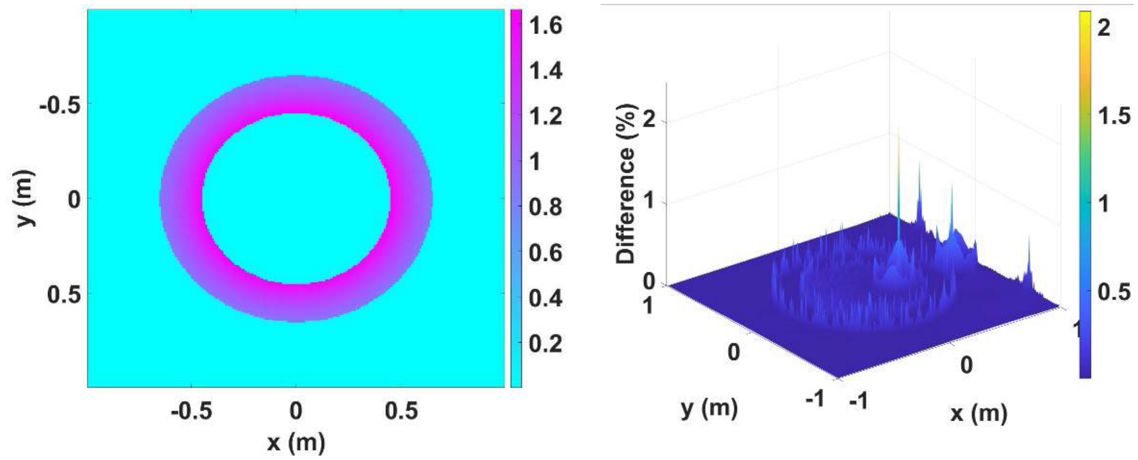

(a) (b)

Fig. 25. Comparison of flux density results for coarser mesh. (a) Flux density results from FEM on coarser mesh (65 025 elements). (b) Difference of the flux density between FEM on coarser mesh (65 025 elements) and KFBIM for Example 2.

The normalized rms difference is computed by

$$\text{Difference}_{\text{NRMS}} = \frac{100\%}{B_{\max,\text{FEM}} - B_{\min,\text{FEM}}} \sqrt{\frac{1}{K}\sum_{k=1}^{K}\left(B_{k,\text{FEM}} - B_{k,\text{KFBIM}}\right)^2} \quad (86)$$

and found to be 0.046%, 0.022%, and 0.015% for the three comparisons mentioned above. Apparently, the closest result to the KFBIM is the FEM on the densest mesh, and with increasing mesh density, the result becomes closer.

Next, the values calculated on the boundary are compared between KFBIM and FEM. Figs. 19 and 20 show the vector potential comparison. The tangential field intensity is also compared to the boundaries in Figs. 21 and 22. For a 256 × 256 grid, there are 181 and 261 points on the inner and outer boundaries, respectively. The results of 300 points from FEM

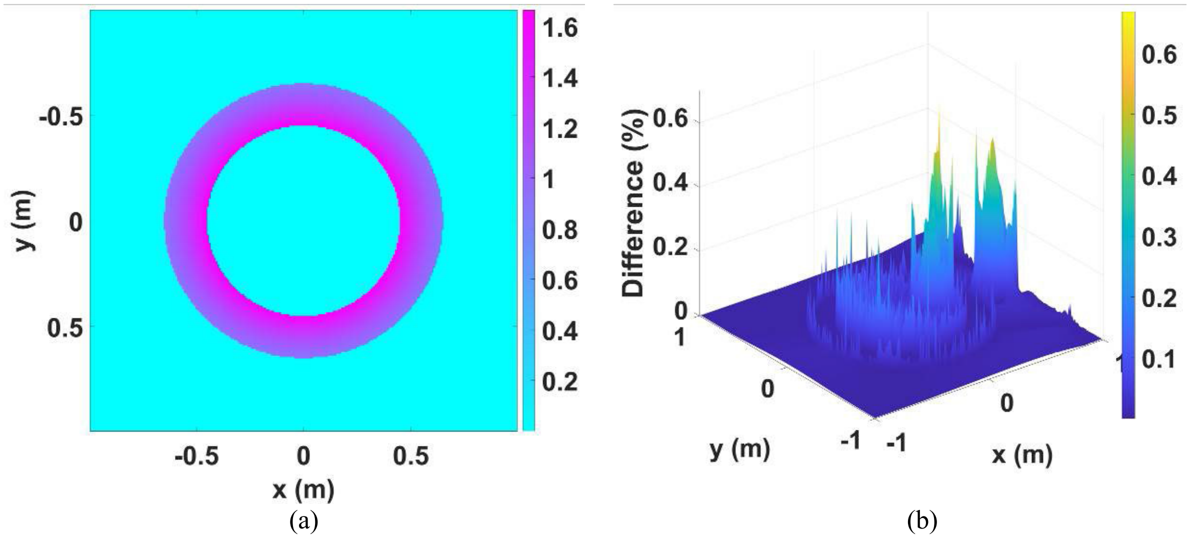

Fig. 26. Comparison of flux density results for dense mesh. (a) Flux density results from FEM on dense mesh (261 121 elements). (b) Difference of the flux density between FEM on dense mesh (261 121 elements) and KFBIM for Example 2.

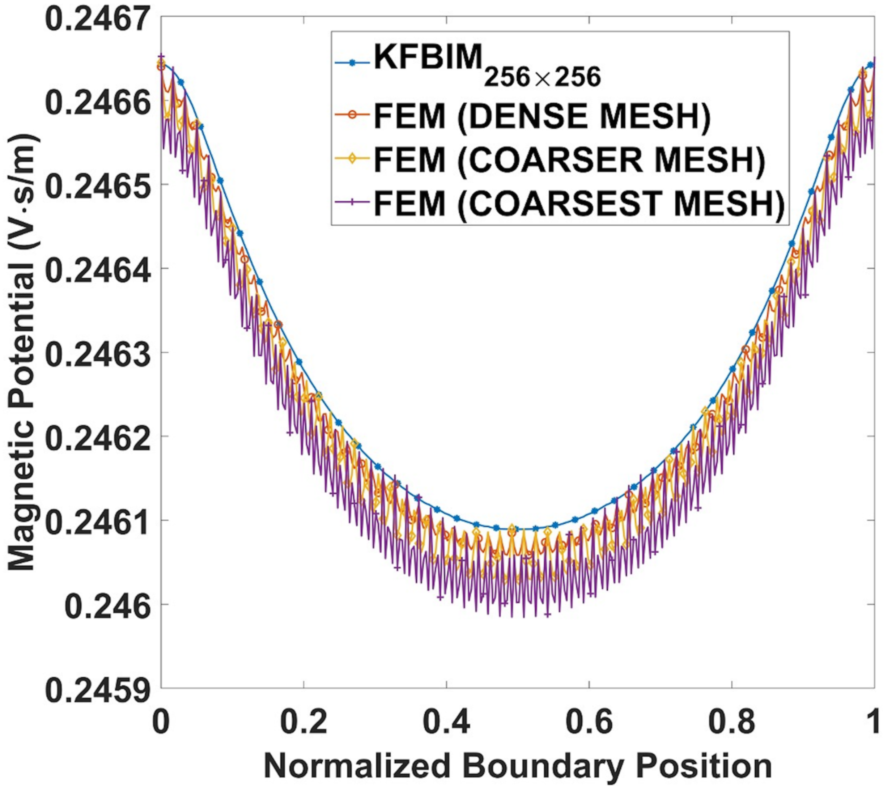

Fig. 27. Comparison of the magnetic potential on the inner boundary between KFBIM (256 × 256) (almost no oscillations) and FEM (more oscillations) for Example 2.

are taken for the inner boundary and the outer boundary. In Fig. 23, a sample of double- or single-layer densities is presented for the boundary, which cannot be extracted from the FEM data.

Example 2 (Nonhomogeneous Permeable Material): For this example, the relative permeability on the toroidal core is spatially variable $(5000/1 + 2(x^2 + y^2)) + 200$, as mentioned in Section IV. These accuracy comparisons for this problem include flux density, boundary magnetic potential, and boundary field intensity, which uses the same setup as the first example. The point-by-point difference and rms difference are calculated using the same definitions as the first example as (85) and (86). The point-by-point differences are shown in Figs. 24–26, and the maximum differences are 6.83%, 2.09%, and 0.67%, respectively. The normalized rms differences are 0.03%, 0.017%, and 0.008%, respectively.

Figs. 27 and 28 show the vector potential comparison. The tangential field intensity is also compared to the boundaries in

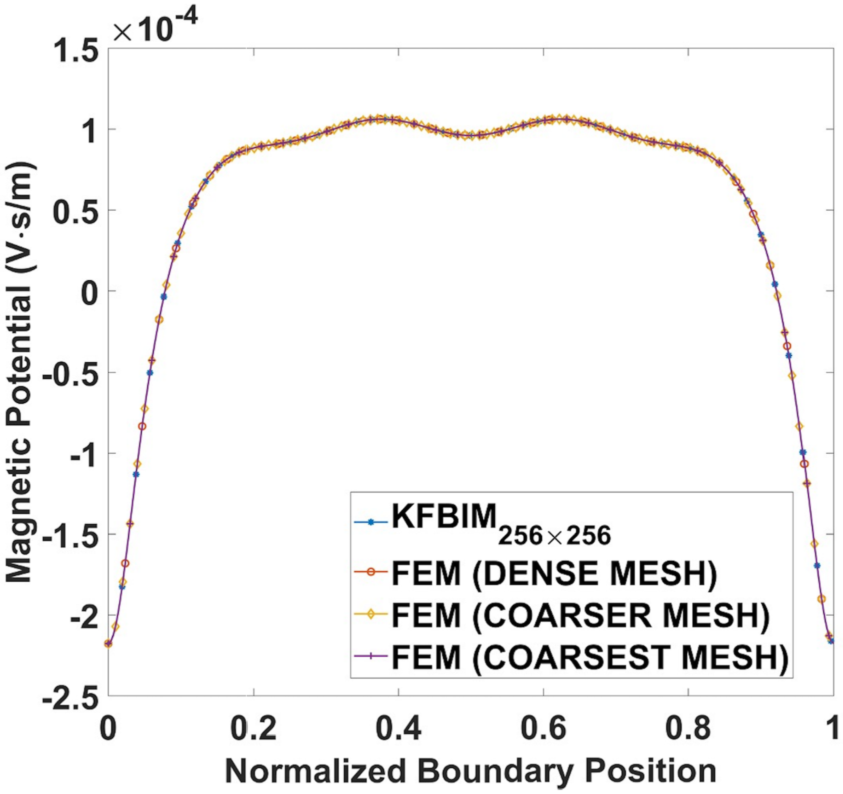

Fig. 28. Comparison of the magnetic potential on the outer boundary between KFBIM (256 × 256) and FEM for Example 2.

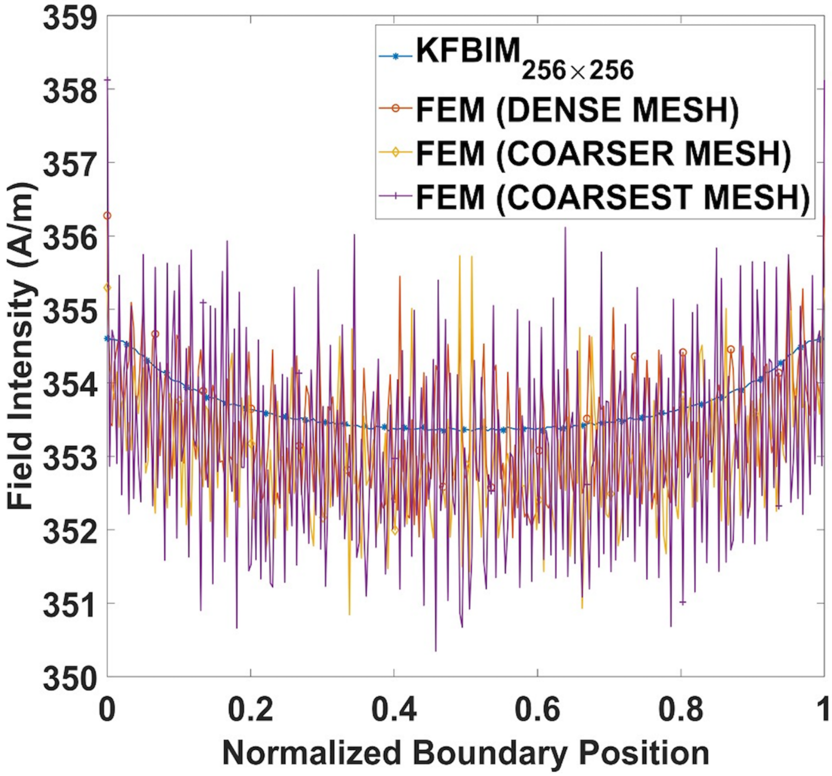

Fig. 29. Comparison of the tangential field intensity on the inner boundary between KFBIM (256 × 256) (almost no oscillations) and FEM (more oscillations) for Example 2.

Figs. 29 and 30. In Fig. 31, the sample of double- or single-layer densities is presented for the boundary as well.

Based on the accuracy comparisons of the two examples, the results of point-by-point field density solved from KFBIM agree with FEM very well, and it is shown that KFBIM with coarser mesh can have the same accuracy level of FEM with denser mesh. The difference is less than 1%. However, for the magnetic potential and field intensity on the boundaries,

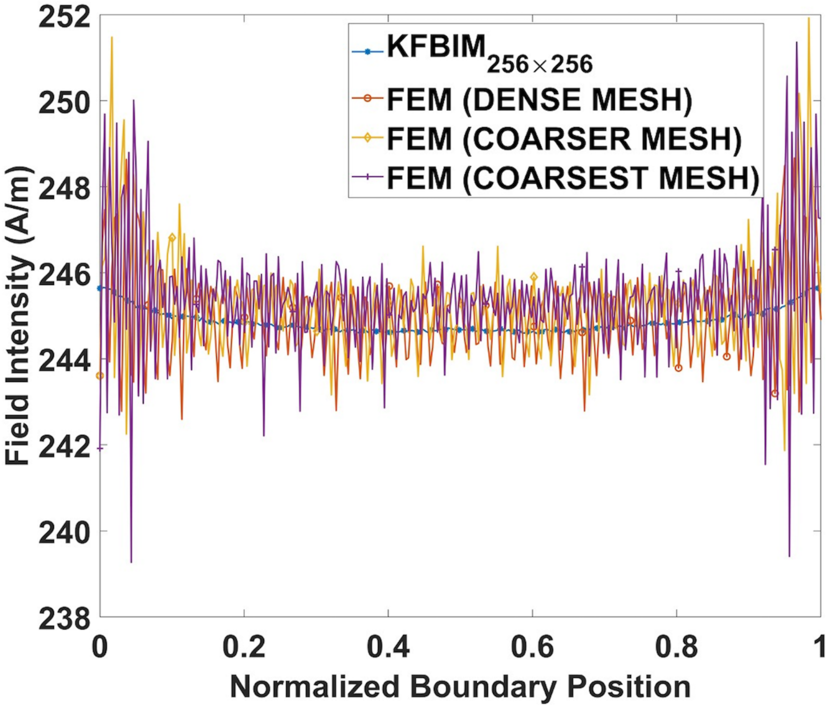

Fig. 30. Comparison of the tangential field intensity on the outer boundary between KFBIM (256 × 256) (almost no oscillations) and FEM (more oscillations) for Example 2.

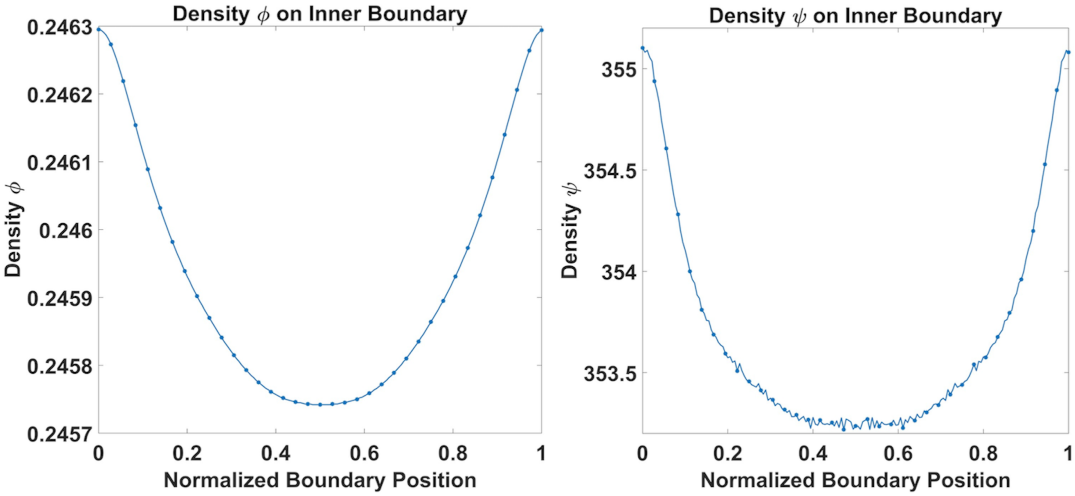

Fig. 31. Densities on the inner and outer boundaries computed by KFBIM for Example 2.

the KFBIM does a better job than FEM because the KFBIM results are smoother than those from FEM (which tends to oscillate). Instead of solving the unknown values on the boundaries, such as KFBIM, FEM solves for unknown values in the domain, so the values on the boundaries are interpolated from the calculated values on each mesh node by the FEM software. Thus, the values on the boundaries from FEM tend to oscillate. In addition, the results of double- or single-layer densities at the boundary can be obtained as well.

D. Efficiency Comparison

All numerical computations for both KFBIM and FEM are performed on a computer with Intel[1] Core[2] i5-8400 CPU @ 2.8 GHz and 12.0 GB RAM. For KFBIM, comparisons of computation time (measured in CPU seconds) between different grids for two examples are shown in Table II. The computation CPU time is almost linearly proportional to the number of grid nodes. The computation time of FEM for the two problems solved on different grids is summarized in Table III. For the coarser mesh, the KFBIM is faster than FEM. However, for the dense mesh that we compared, the computational time of those two methods is almost the same.

It should be noted that the KFBIM with a coarser mesh can solve the problem with at least the same level of accuracy as the FEM with the denser mesh, as shown in Section V-C. It takes 25.78 and 28.00 s for KFBIM to solve Example 1 and Example 2, respectively, using the 256×256 grid. However, for FEM (ANSYS), it takes 114.04 and 131.60 s to solve Example 1 and Example 2, respectively, using the denser mesh,

---

[1] Registered trademark.

[2] Trademarked.

TABLE II

CPU CLOCK TIME OF KFBIM

Grid (KFBIM)	Time (s) (Example 1)	Time (s) (Example 2)
128×128	5.78	6.31
256×256	25.78	28.00
512×512	115	129.79

TABLE III

CPU CLOCK TIME OF FEM (ANSYS)

Grid (FEM)	Time (s) (Example 1)	Time (s) (Example 2)
16027 elements	19.46	20.80
68439 elements	39.46	44.14
268535 elements	114.04	131.60

which could reach the accuracy of the KFBIM. In other words, it takes more time for FEM to get the same level of accuracy as KFBIM, which confirms that KFBIM is computationally more efficient of the two approaches. This benefit can be particularly significant in complex geometries, such as electric machines, where iterative designs and optimization are often needed. However, these cases also introduce two additional problems, which can be challenging: the first is a moving boundary, and the second is the analytical description of a sharp edge. These two aspects are currently being investigated and will be presented in subsequent publications.

This study shows that not only can the constant permeability material problem be solved by KFBIM shown in Example 1, but Example 2 also shows that the nonhomogeneous permeable material problem can be solved accurately and efficiently by KFBIM, which is one of the advantages of KFBIM as well compared to other traditional boundary integral methods. Incorporating the impact of material with the B–H curve may need some additional techniques, such as supine interpolation and proper iterative methods coupled to find the proper permeability for the material at each location based on the B–H curve, which is an extension of this work. While the 3-D application is not the current focus of this article, the work has been reported in this space [4]. The 3-D framework of the kernel-free boundary integral method has been developed for boundary value problems [4], but the interface problem solver is still underdeveloped. Since the 2-D results of the magnetostatics problem are encouraging, the immediate future work would be to finish the 3-D solver for interface problems and apply the 3-D solver for the magnetostatics problems, where the B–H curve will be incorporated into the framework as well.

VI. CONCLUSION

This article presents a comprehensive study of a kernel-free boundary integral method and explores its effectiveness in solving PDEs for 2-D magnetostatic field analysis. In this study, KFBIM is used to solve the electromagnetics problem on a toroidal core for both constant permeability material and non-homogeneous material, and the results are compared with commercial FEM software. Based on the results, the KFBIM is found to be at least as accurate as FEM, with much better computational efficiency. A finite difference method is used in KFBIM, so it does not require a body-fit mesh. Also, the finite difference method is coupled with numerical corrections and based on the integral formulation to produce a well-conditioned discrete linear system. Thus, KFBIM gains high accuracy and improved computational efficiency simultaneously. The proposed analysis has been carried out for a toroidal inductor core, which is commonly used in inductor and transformer designs. It forms the first step for application toward more complex geometries and applications such as electric machines. The high accuracy and computational efficiency of KFBIM are very important to the multi-objective optimization within the field of electromechanics for complex geometries because a single design often needs to be optimized iteratively. Therefore, KFBIM can potentially be used as an alternative method in the analysis of electromagnetics problems, especially in the optimization of electric machine designs, and can serve as a valuable tool for design engineers. This approach is currently under development for application-specific design; such an approach will be very useful for practicing engineers tasked with the design of size-constrained electromagnetic transducers. Subsequent publications will present the use of this approach for such designs.

APPENDIX A
PDE DISCRETIZATION

Let box $\mathcal{B} = [a, b] \times [c, d]$. N is the mesh size on each axis direction. $h_x = (b - a/N)$; $h_y = (d - c/N)$. Assume that $h_x = h_y = h$ for simplicity. $x_i = a + ih$; $y_j = c + jh$; $\mathbf{p}_{i,j} = (x_i, y_j)$, $i, j = 0, 1, \ldots, N$. The PDE is discretized $\mathcal{A}v \equiv \nabla \cdot (\nu(\mathbf{p})\nabla v) = f$ in $\mathcal{B}\backslash\Gamma$ on the Cartesian grid with a modified finite difference scheme

$$\mathcal{A}_h v_{i,j} \equiv \frac{s_{i,j} - 4\bar{\nu}_{i,j} v_{i,j}}{h^2} = f_{i,j} \tag{87}$$

$$\begin{aligned} s_{i,j} = {} & \nu_{i+\frac{1}{2},j} v_{i+1,j} + \nu_{i-\frac{1}{2},j} v_{i-1,j} + \nu_{i,j+\frac{1}{2}} v_{i,j+1} \\ & + \nu_{i,j-\frac{1}{2}} v_{i,j-1} \end{aligned} \tag{88}$$

$$\bar{\sigma}_{i,j} = \frac{\nu_{i+\frac{1}{2},j} + \nu_{i-\frac{1}{2},j} + \nu_{i,j+\frac{1}{2}} + \nu_{i,j-\frac{1}{2}}}{4} \tag{89}$$

where $v_{i,j}$ is a finite difference approximation of $v(\mathbf{p}_{i,j})$, $\nu_{i+(1/2),j} = \nu(x_i + h/2, y_j)$, $\nu_{i-(1/2),j} = \nu(x_i - h/2, y_j)$, $\nu_{i,j+(1/2)} = \nu(x_i, y_j + h/2)$, $\nu_{i,j-(1/2)} = \nu(x_i, y_j - h/2)$, and $f_{i,j} = f(x_i, y_j)$. The finite difference scheme here is based on a five-point stencil. Equation (76) has a second-order accuracy if without discontinuities across Γ.

APPENDIX B
CORRECTION IN DISCRETE SYSTEM

If a node $\mathbf{p}_{i,j}$ and any of its neighbors $\mathbf{p}_{i+1,j}$, $\mathbf{p}_{i-1,j}$, $\mathbf{p}_{i,j+1}$, and $\mathbf{p}_{i,j-1}$ are on different sides of Γ, we call $\mathbf{p}_{i,j}$ as an irregular node. Otherwise, $\mathbf{p}_{i,j}$ is a regular node. The truncation error of the finite difference method is large at those irregular nodes. If (x_i, y_j) is a regular point, $\mathcal{A}_h v(x_i, y_j) - f(x_i, y_j) = O(h^2)$; if (x_i, y_j) is an irregular point, $\mathcal{A}_h v(x_i, y_j) - f(x_i, y_j) = O(h^{-2})$. The scheme needs to be corrected at irregular points to keep the second-order accuracy on the whole mesh. The

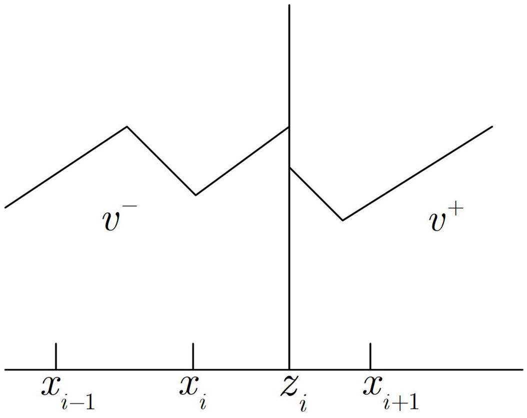

Fig. 32. Irregular node.

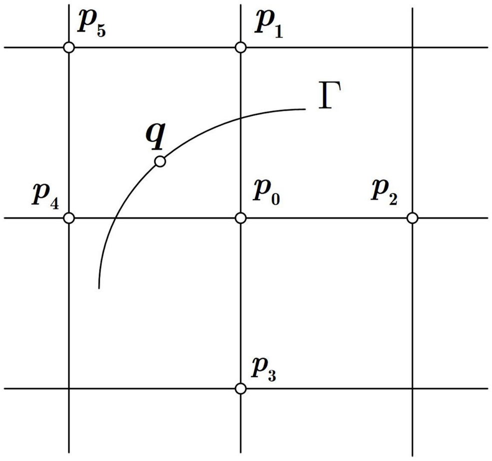

Fig. 33. Interpolation points' selection.

correction procedure using a simple case is shown in Fig. 32, where Γ intersects a horizontal grid line at (z_i, y_j), $x_i \le z_i < x_{i+1}$.

The local truncation error is

$$\begin{aligned} E_{h,x}(x_i, y_j) \equiv\ & \frac{\nu_{i+\frac{1}{2},j}\left(v^+(x_{i+1}, y_j) - v^-(x_i, y_j)\right)}{h^2} \\ & - \frac{\nu_{i-\frac{1}{2},j}\left(v^-(x_i, y_j) - v^-(x_{i-1}, y_j)\right)}{h^2} \\ & - \frac{\partial}{\partial x}\left(\nu \frac{\partial}{\partial x} v^-(x_i, y_j)\right) \end{aligned} \tag{90}$$

and $v^\pm(x_{i+1}, y_j)$ is $v^\pm(x_{i+1}, y_j)$ expanded at (z_i, y_j) using a Taylor expansion at the z_i point as

$$\begin{aligned} v^\pm(x_{i+1}, y_j) = v^\pm(z_i, y_j) &+ \partial_x v^\pm(z_i, y_j)(x_{i+1} - z_i) \\ &+ \frac{1}{2}\partial_{xx} v^\pm(z_i, y_j)(x_{i+1} - z_i)^2 \\ &- \frac{1}{6}\partial_{xxx} v^\pm(z_i, y_j)(x_{i+1} - z_i)^3 + O(h^4). \end{aligned} \tag{91}$$

The truncation error derived at (x_i, y_j) is

$$\begin{aligned} & E_{h,x}(x_i, y_j) \\ & \equiv \frac{\nu_{i+\frac{1}{2},j}\left(v^+(x_{i+1}, y_j) - v^-(x_i, y_j)\right)}{h^2} \\ & = \frac{\nu_{i-\frac{1}{2},j}}{h^2}\left\{[v] + [v_x](x_{i+1} - z_i) + \frac{1}{2}[v_{xx}](x_{i+1} - z_i)^2 \right. \\ & \qquad \left. + \frac{1}{6}[v_{xxx}](x_{i+1} - z_i)^3\right\} + O(h^2). \end{aligned} \tag{92}$$

In this equation, $[v] = v^+(z_i, y_j) - v^-(z_i, y_j)$, $[v_x] = \partial_x v^+(z_i, y_j) - \partial_x v^-(z_i, y_j)$, $[v_{xx}] = \partial_{xx} v^+(z_i, y_j) - \partial_{xx} v^-(z_i, y_j)$, and $[v_{xxx}] = \partial_{xxx} v^+(z_i, y_j) - \partial_{xxx} v^-(z_i, y_j)$ are jumps of v value and its partial derivatives across the interface Γ.

Then, a correction term is added on the right-hand side of the finite difference equation as

$$C^+_{h,x}(x_i, y_j) = \frac{\nu_{i+\frac{1}{2},j}\left\{[v] + [v_x](x_{i+1} - z_i) + \frac{1}{2}[v_{xx}](x_{i+1} - z_i)^2\right\}}{h^2}. \tag{93}$$

The computation of jumps $[v]$, $[v_x]$, and $[v_{xx}]$ are given in Appendix E. Similarly, if a horizontal gird line intersects Γ between x_{i-1} and x_i, a correction term is added as

$$\begin{aligned} & C^-_{h,x}(x_i, y_j) \\ & = -\frac{\nu_{i-\frac{1}{2},j}\left\{[v] + [v_x](x_{i-1} - z_i) + \frac{1}{2}[v_{xx}](x_{i-1} - z_i)^2\right\}}{h^2}. \end{aligned} \tag{94}$$

Γ may intersect grid lines horizontally and vertically multiple times. For every intersection point, necessary correction terms are added among $C^+_{h,x}$, $C^-_{h,x}$, $C^+_{h,y}$, and $C^-_{h,y}$ on the right-hand side of (87). $C_h(x_i, y_j)$ is denoted as a summation of all corrections at (x_i, y_j). Then, a modified finite difference equation is summarized. If (x_i, y_j) is a regular point, $\mathcal{A}_h v_{i,j} = f_{i,j}$, and if (x_i, y_j) is an irregular point, $\mathcal{A}_h v_{i,j} = f_{i,j} + C_h(x_i + y_j)$. The finite difference method here has a second-order accuracy except at irregular points, where first-order accuracy is expected. However, as shown in [6] and [7], the solution to the corrected linear system has a second-order accuracy.

APPENDIX C
SOLUTION OF THE DISCRETE FINITE DIFFERENCE EQUATIONS

The coefficient matrix created by the finite difference method is a symmetric positive definite matrix because of its diagonal dominance. For a constant coefficient PDE, i.e., the Laplacian or modified Helmholtz operator, a fast Fourier transform-based elliptic PDE solver can be used to solve (93) efficiently. For a PDE with variable coefficients, we implement a GMG-PCG [10], [11]. The whole routine is a full multigrid process where a preconditioned conjugate gradient iterative method is coupled with every single V-cycle, while the preconditioning is a single multigrid V cycle process. The pre-smoothing and the post-smoothing are one forward and one backward Gauss–Seidel iterations. The prolongation is calculated by a bi-linear interpolation, and the restriction is the adjoint of the prolongation. The coarsest grid has only one point inside box $\mathcal{B}$.

APPENDIX D
INTERPOLATION OF INTEGRALS ON THE INTERFACE

Assume that v_h is a piecewise smooth function that satisfies the PDE operator $\mathcal{A}$. It has discontinuities of function value and partial derivatives across Γ. Let $v_h(\mathbf{p}_{i,j}) = v_{i,j}$; here, $v_{i,j}$ is the numerical solution given by the finite difference method. $v_h(\mathbf{p})$ is expanded on one point $\mathbf{q} \in \Gamma$

$$\begin{aligned} v_h(\mathbf{p}) = {} & v_h^+(\mathbf{q}) + \frac{\partial v_h^+(\mathbf{q})}{\partial x}\xi + \frac{\partial v_h^+(\mathbf{q})}{\partial y}\eta \\ & + \frac{1}{2}\frac{\partial^2 v_h^+(\mathbf{q})}{\partial x^2}\xi^2 + \frac{\partial^2 v_h^+(\mathbf{q})}{\partial x \partial y}\xi\eta + \frac{1}{2}\frac{\partial^2 v_h^+(\mathbf{q})}{\partial y^2}\eta^2 \\ & + O\left(|\mathbf{p}-\mathbf{q}|^3\right) \quad \text{if } \mathbf{p} \in \Omega_i \end{aligned} \tag{95}$$

and

$$\begin{aligned} v_h(\mathbf{p}) = {} & v_h^-(\mathbf{q}) + \frac{\partial v_h^-(\mathbf{q})}{\partial x}\xi + \frac{\partial v_h^-(\mathbf{q})}{\partial y}\eta \\ & + \frac{1}{2}\frac{\partial^2 v_h^-(\mathbf{q})}{\partial x^2}\xi^2 + \frac{\partial^2 v_h^-(\mathbf{q})}{\partial x \partial y}\xi\eta + \frac{1}{2}\frac{\partial^2 v_h^-(\mathbf{q})}{\partial y^2}\eta^2 \\ & + O(|\mathbf{p}-\mathbf{q}|^3) \quad \text{if } \mathbf{p} \in \Omega_e \end{aligned} \tag{96}$$

where v_h^+ and v_h^- are restrictions of v_h in Ω_i and Ω_e, and $(\xi, \eta) = \mathbf{p} - \mathbf{q}$. The way to choose six grid nodes around $\mathbf{q}$ is given as follows. First, the closest mesh point $\mathbf{p}_0$ is picked to $\mathbf{q}$. Then, four neighbors of $\mathbf{p}_0$ are chosen correspondingly. $\mathbf{p}_5$ is the last one to construct a small rectangle, which contains $\mathbf{q}$ as shown in Fig. 33.

For brevity, the restriction of v_h and its partial derivative are denoted as $V^\pm \equiv v_h^\pm(\mathbf{q})$, $V_x^\pm \equiv (\partial v_h^\pm(\mathbf{q})/\partial x)$, $V_y^\pm \equiv (\partial v_h^\pm(\mathbf{q})/\partial y)$, $V_{xx}^\pm \equiv (\partial^2 v_h^\pm(\mathbf{q})/\partial x^2)$, $V_{xy}^\pm \equiv (\partial^2 v_h^\pm(\mathbf{q})/\partial x \partial y)$, and $V_{yy}^\pm \equiv (\partial^2 v_h^\pm(\mathbf{q})/\partial y^2)$. They are limit values from the corresponding side, i.e., $V^+ = \lim_{\mathbf{p}' \to \mathbf{q}} v_h(\mathbf{p}')$, $\mathbf{p}' \in \Omega_i$. $v_h(\mathbf{p})$ is represented as $V^+ + V_x^+\xi_j + V_y^+\eta_j + (1/2)\xi_j^2 V_{xx}^+ + V_{xy}^+\xi_j\eta_j + (1/2)V_{yy}^+\eta_j^2 = V_j$ if $\mathbf{p}_j \in \Omega_i$; if $\mathbf{p}_j \in \Omega_e$, $V^- + V_x^-\xi_j + V_y^-\eta_j + (1/2)\xi_j^2 V_{xx}^- + V_{xy}^-\xi_j\eta_j + (1/2)V_{yy}^-\eta_j^2 = V_j$. Besides, $J_j = [V] + [V_x]\xi_j + [V_y]\eta_j + (1/2)[V_{xx}]\xi_j^2 + [V_{xy}]\xi_j\eta_j + (1/2)[V_{yy}]\eta_j^2$ is denoted and reorganized into $V^+ + V_x^+\xi_j + V_y^+\eta_j + (1/2)\xi_j^2 V_{xx}^+ + V_{xy}^+\xi_j\eta_j + (1/2)V_{yy}^+\eta_j^2 = V_j + J_j$, for $j = 0, 1, \ldots, 5$; here, $(\xi_j, \eta_j) = \mathbf{p}_j - \mathbf{q}$ and $V_j = v_h(\mathbf{p}_j)$. There are six unknowns V^+, V_x^+, V_y^+, V_{xx}^+, V_{xy}^+, and V_{yy}^+ for each boundary node $\mathbf{q}$. Also, there are six equations to solve them. After jumps are computed (details given in Appendix E), it is straightforward to solve a 6×6 linear system.

APPENDIX E
COMPUTE JUMPS OF PARTIAL DERIVATIVES

Assume that $v(\mathbf{p})$ satisfies the interface problem

$$\mathcal{A}v \equiv \nabla \cdot (\nu \nabla v) = f \quad \text{in } \mathcal{B}\backslash\Gamma \tag{97}$$

$$[v] = \varphi \quad \text{on } \Gamma \tag{98}$$

$$[\nu \partial_{\mathbf{n}} v] = \psi \quad \text{on } \Gamma. \tag{99}$$

The parametric description of Γ is considered as follows: $x = x(\theta)$ and $y = y(\theta)$. The tangent and normal vectors are given, respectively, by $\tau = (x_\theta, y_\theta)$ and $\mathbf{n} = ((y_\theta/(x_\theta^2 + y_\theta^2)^{1/2}), (-x_\theta/(x_\theta^2 + y_\theta^2)^{1/2}))$; here, $x_\theta = (\partial x/\partial\theta)$ and $y_\theta = (\partial y/\partial\theta)$. Meanwhile, $\partial_\tau = \tau_1(\partial/\partial x) + \tau_2(\partial/\partial y)$ and $\partial_{\mathbf{n}} = \mathbf{n}_1(\partial/\partial x) + \mathbf{n}_2(\partial/\partial y)$ are denoted. Tangential derivative of (98) is taken on Γ to be $\partial_\tau[v] = \partial_\tau\varphi$, and the right-hand side is expanded as $\partial_\tau\varphi = x_\theta\varphi_x + y_\theta\varphi_y = \varphi_\theta$. Also, $\mathbf{n}_1[v_x] + \mathbf{n}_2[v_y] = (\psi/\nu)$ and $x_\theta[v_x] + y_\theta[v_y] = \varphi_\theta$ are derived; after solving these two equations, $[v_x]$ and $[v_y]$ are obtained. These two jumps are plugged into (97) on Γ to be $\nabla \cdot (\nu\nabla[v]) - \kappa[v] = [f]$, and it is expanded to get $\nu_x[v_x] + \nu[v_{xx}] + \nu_y[v_y] + \nu[v_{yy}] = [f]$. The double tangential derivative of (98) is taken on Γ to be $\partial_{\tau\tau}[v] = \partial_{\tau\tau}\varphi$, and it is equivalent to $x_\theta^2[v_{xx}] + y_\theta^2[v_{xx}] + 2x_\theta y_\theta[v_{xy}] + (x_\theta(\partial x_\theta/\partial x) + y_\theta(\partial x_\theta/\partial y))[v_x] + (x_\theta(\partial y_\theta/\partial x) + y_\theta(\partial y_\theta/\partial y))[v_y] = \varphi_{\theta\theta}$; here, $\varphi_{\theta\theta} = (\partial^2\varphi/\partial\theta^2)$, $x_{\theta\theta} = (\partial^2 x/\partial\theta^2)$, and $y_{\theta\theta} = (\partial^2 y/\partial\theta^2)$. The tangential derivative of (99) is taken on Γ, $\partial_\tau\{[\nu\partial_{\mathbf{n}}v]\} = \partial_\tau\psi$, and it is expanded as

$$\begin{aligned} \psi_\theta = {} & \mathbf{n}_1[v_x]\left(\nu_x x_\theta + \nu_y y_\theta\right) + \mathbf{n}_2\left[v_y\right]\left(\nu_x x_\theta + \nu_y y_\theta\right) \\ & + \nu[v_x]\left(x_\theta\frac{\partial\mathbf{n}_1}{\partial x} + y_\theta\frac{\partial\mathbf{n}_1}{\partial y}\right) \\ & + \nu\left[v_y\right]\left(x_\theta\frac{\partial\mathbf{n}_2}{\partial x} + y_\theta\frac{\partial\mathbf{n}_2}{\partial y}\right) + \nu\mathbf{n}_1 x_\theta[v_{xx}] + \nu\mathbf{n}_2 y_\theta\left[v_{yy}\right] \\ & + \nu\left[v_{xy}\right](\mathbf{n}_1 y_\theta + \mathbf{n}_2 x_\theta). \end{aligned}$$

The following equations are derived:

$$\begin{aligned} & [v_{xx}] + \left[v_{yy}\right] \\ & \quad = \left\{-\sigma_x[v_x] - \sigma_y\left[v_y\right] + \left[f\right]\right\}/\nu \end{aligned} \tag{100}$$

$$\begin{aligned} & x_\theta^2[v_{xx}] + y_\theta^2\left[v_{yy}\right] + 2x_\theta y_\theta\left[v_{xy}\right] \\ & \quad = \varphi_{\theta\theta} - x_{\theta\theta}[v_x] - y_{\theta\theta}\left[v_y\right] \end{aligned} \tag{101}$$

$$\begin{aligned} & \mathbf{n}_1 x_\theta[v_{xx}] + \mathbf{n}_2 y_\theta\left[v_{yy}\right] + \left[v_{xy}\right](\mathbf{n}_1 y_\theta + \mathbf{n}_2 x_\theta) \\ & \quad = \frac{\psi_\theta}{\nu} - \frac{\sigma_\theta}{\nu}\{\mathbf{n}_1[v_x] + \mathbf{n}_2\left[v_y\right]\} - \frac{\partial\mathbf{n}_1}{\partial\theta}[v_x] - \frac{\partial\mathbf{n}_2}{\partial\theta}\left[v_y\right]_3. \end{aligned} \tag{102}$$

$[v_{xx}]$, $[v_{xy}]$, and $[v_{yy}]$ are obtained after solving these three equations.

ACKNOWLEDGMENT

This work was supported by the National Science Foundation, Division of Electrical, Communications and Cyber Systems, under Grant ECCS-1927432.

REFERENCES

[1] ANSYS. *ANSYS Maxwell*. Accessed: Jun. 4, 2022. [Online]. Available: https://www.ansys.com/products/electronics/ansys-maxwell

[2] COMSOL. *AC/DC Module*. Accessed: Jun. 4, 2022. [Online]. Available: https://www.comsol.com/acdc-module

[3] Y. Xie and W. Ying, "A fourth-order kernel-free boundary integral method for the modified Helmholtz equation," *J. Sci. Comput.*, vol. 78, no. 3, pp. 1632–1658, Sep. 2018.

[4] Y. Xie and W. Ying, "A fourth-order kernel-free boundary integral method for implicitly defined surfaces in three space dimensions," *J. Comput. Phys.*, vol. 415, Aug. 2020, Art. no. 109526.

[5] Y. Xie, W. Ying, and W.-C. Wang, "A high-order kernel-free boundary integral method for the biharmonic equation on irregular domains," *J. Sci. Comput.*, vol. 80, no. 3, pp. 1681–1699, Jul. 2019.

[6] W. Ying and C. S. Henriquez, "A kernel-free boundary integral method for elliptic boundary value problems," *J. Comput. Phys.*, vol. 227, no. 2, pp. 1046–1074, Dec. 2007.

[7] W. Ying and W.-C. Wang, "A kernel-free boundary integral method for variable coefficients elliptic PDEs," *Commun. Comput. Phys.*, vol. 15, no. 4, pp. 1108–1140, Apr. 2014.

[8] W. Ying and W.-C. Wang, "A kernel-free boundary integral method for implicitly defined surfaces," *J. Comput. Phys.*, vol. 252, pp. 606–624, Nov. 2013.

[9] H. C. Karmaker and S. D. T. Robertson, “Integral equation formulation for the solution of magnetic field problems Part—II: Magnetization vector approach,” *IEEE Trans. Power App. Syst.*, vol. PAS-92, no. 2, pp. 815–823, Mar. 1973.

[10] Y. Saad and M. H. Schultz, “GMRES: A generalized minimal residual algorithm for solving nonsymmetric linear systems,” *SIAM J. Sci. Statist. Comput.*, vol. 7, no. 3, pp. 856–869, 1986.

[11] Y. Saad, *Iterative Methods for Sparse Linear Systems*. Boston, MA, USA: PWS, 1996.

[12] N. Normann, F. Borgermann, and H. Mende, “Simple boundary element method for three-dimensional magnetostatic problems,” *IEEE Trans. Magn.*, vol. MAG-21, no. 3, pp. 1235–1239, May 1985.

[13] W. M. Rucker, C. Magele, E. Schlemmer, and K. R. Richter, “Boundary element analysis of 3-D magnetostatic problems using scalar potentials,” *IEEE Trans. Magn.*, vol. 28, no. 2, pp. 1099–1102, Mar. 1992.

[14] J. Peng, S. Salon, and M. Chari, “A comparison of finite element and boundary element formulations for three-dimensional magnetostatic problems,” *IEEE Trans. Magn.*, vol. MAG-20, no. 5, pp. 1950–1952, Sep. 1984.

[15] A. D. Brovont, “A Galerkin boundary element method for two-dimensional nonlinear magnetostatics,” Ph.D. dissertation, School Elect. Comput. Eng., Purdue Univ., West Lafayette, IN, USA, 2016.

[16] F. Paris and J. Canas, *Boundary Element Method—Fundamentals and Applications*. Oxford, U.K.: Oxford Univ. Press, 1997.

[17] O. Chadebec, J.-L. Coulomb, and F. Janet, “A review of magnetostatic moment method,” *IEEE Trans. Magn.*, vol. 42, no. 4, pp. 515–520, Apr. 2006.

[18] R. Harrington, “Origin and development of the method of moments for field computation,” *IEEE Antennas Propag. Mag.*, vol. 32, no. 3, pp. 31–35, Jun. 1990.

[19] F. Janet, J. L. Coulomb, C. Chillet, and P. Mas, “Magnetic moment and reluctance network mixed method applied to transformer modeling,” *IEEE Trans. Magn.*, vol. 41, no. 5, pp. 1428–1431, May 2005.

[20] D. Horvath, R. Howard, and S. Pekarek, “Lorentz force/torque calculation in 2-D method of moments,” *IEEE Trans. Magn.*, vol. 56, no. 8, pp. 1–8, Aug. 2020.

[21] S. Li, J. S. Lowengrub, and P. H. Leo, “A rescaling scheme with application to the long-time simulation of viscous fingering in a Hele–Shaw cell,” *J. Comput. Phys.*, vol. 225, no. 1, pp. 554–567, Jul. 2007.

[22] S. Li and X. Li, “A boundary integral method for computing the dynamics of an epitaxial island,” *SIAM J. Sci. Comput.*, vol. 33, no. 6, pp. 3282–3302, Jan. 2011.

[23] A. K. Barua, S. Li, H. Feng, X. Li, and J. Lowengrub, “An efficient rescaling algorithm for simulating the evolution of multiple elastically stressed precipitates,” *Commun. Comput. Phys.*, vol. 14, no. 4, pp. 940–959, Oct. 2013.

[24] Y. Cao, Y. Xie, M. Krishnamurthy, S. Li, and W. Ying, “A kernel-free boundary integral method for elliptic PDEs on a doubly connected domain,” *J. Eng. Math.*, vol. 136, no. 1, pp. 2–22, Aug. 2022.

[25] OD. Kellogg, *Foundations of Potential Theory*. Berlin, Germany: Springer, 1929.

[26] D. Colton, *Partial Differential Equations*. New York, NY, USA: Random House, 1988.

[27] R. Kress, *Linear Integral Equations*. Berlin, Germany: Springer, 1989.

[28] K. E. Atkinson, *The Numerical Solution of Integral Equations of the Second Kind*. Cambridge, U.K.: Cambridge Univ. Press, 1997.

[29] W. McLean, *Strongly Elliptic Systems and Boundary Integral Equations*. Cambridge, U.K.: Cambridge Univ. Press. 2000.

[30] A. Eroglu, “Complete modeling of toroidal inductors for high power RF applications,” *IEEE Trans. Magn.*, vol. 48, no. 11, pp. 4526–4529, Nov. 2012.